Published in Reviews in Mineralogy, Yakymchuk, C., Clark, C., & White, R. W. (2017). Phase Relations, Reaction Sequences and Petrochronology. Reviews in Mineralogy and Geochemistry, 83(1), 13–53. https://doi.org/10.2138/rmg.2017.83.2

2 Phase Relations, Reaction Sequences and Petrochronology

Chris Yakymchuk
Department of Earth and Environmental Sciences
University of Waterloo
Waterloo, Ontario, Canada, N2L 3G1
cyakymchuk@uwaterloo.ca

Chris Clark
Department of Applied Geology
Curtin University
Perth, Western Australia, Australia, 6102

Richard W. White
Earth System Science Research Centre, Institute of Geoscience
University of Mainz
Mainz, Germany, D-55099

INTRODUCTION

At the core of petrochronology is the relationship between geochronology and the petrological evolution of major mineral assemblages. The focus of this chapter is on outlining some of the available strategies to link inferred reaction sequences and microstructures in metamorphic rocks to the ages obtained from geochronology of accessory minerals and datable major minerals. Reaction sequences and mineral assemblages in metamorphic rocks are primarily a function of pressure (*P*), temperature (*T*) and bulk composition (*X*). Several of the major rock-forming minerals are particularly sensitive to changes in *P*–*T* (e.g., garnet, staurolite, biotite, plagioclase), but their direct geochronology is challenging and in many cases not currently possible. One exception is garnet, which can be dated using Sm–Nd and Lu–Hf geochronology (e.g., Baxter et al. 2013). Accessory mineral chronometers such as zircon, monazite, xenotime, titanite and rutile are stable over a relatively wide range of *P*–*T* conditions and can incorporate enough U and/or Th to be dated using U–Th–Pb geochronology. Therefore, linking the growth of *P–T* sensitive major minerals to accessory and/or major mineral chronometers is essential for determining a metamorphic *P–T–t* history, which is itself critical for understanding metamorphic rocks and the geodynamic processes that produce them (e.g., England and Thompson, 1984; McClelland and Lapen 2013; Brown, 2014).

Linking the ages obtained from accessory and major minerals with the growth and breakdown of the important *P–T* sensitive minerals requires an understanding of the metamorphic reaction sequences for a particular bulk rock composition along a well-constrained *P–T* evolution. Fortunately, the phase relations and reaction sequences for the most widely studied metamorphic protoliths (e.g., pelites, greywackes, basalts) can be determined using quantitative phase equilibria forward modelling (e.g., Powell and Holland 2008). Comprehensive activity–composition models of the major metamorphic minerals in large chemical systems (e.g., White et al. 2014a) allow the calculation of phase proportions and compositions for a given rock composition along a metamorphic *P–T* path. For accessory minerals, subsolidus growth and breakdown can be modelled in some cases using phase equilibria modelling (e.g., Spear 2010; Spear and Pyle 2010). Suprasolidus accessory mineral behaviour can be investigated by coupling phase equilibria modelling with the experimental results of accessory mineral solubility in melt (Kelsey et al. 2008; Yakymchuk and Brown 2014b). This technique provides a basic framework for interpreting the geological significance of accessory mineral ages in suprasolidus metamorphic rocks.

In this chapter, we use phase equilibria modelling techniques to investigate the reaction sequences for three common rock types (pelite, greywacke, MORB) along several *P–T* paths and explore how these sequences relate to accessory mineral growth and dissolution with a particular focus on zircon and monazite and to a lesser extent apatite. First, we review the important major rock-forming minerals that are used to link metamorphic reaction sequences to trace element chemistries in accessory minerals. Second, we summarize the current understanding of the controls of accessory mineral growth and breakdown in metamorphic rocks during a *P–T* evolution. Third, we use phase equilibria modelling to examine the reaction sequences for common rock types along several schematic *P–T* paths and discuss the implications for petrochronology. Finally, we examine some of the complicating factors for reconciling the behaviour of accessory minerals in natural systems with the predictions from phase equilibria modelling.

MAJOR MINERALS

Understanding the growth and consumption of the major rock-forming minerals is important in accessory mineral petrochronology for four reasons. First, major minerals may contain significant quantities of the essential structural constituents of accessory minerals commonly used as chronometers. In some cases, accessory mineral can grow directly from the breakdown of major minerals. Examples of this are zircon growth from the release of Zr during the breakdown of garnet (Fraser et al. 1997; Degeling et al. 2001) and ilmenite (Bingen et al. 2001). Second, these minerals may represent important repositories for trace elements, and thus the growth and breakdown of major minerals will influence the availability of these elements for incorporation by growing accessory minerals. Third, the major minerals are important hosts for inclusions of accessory minerals. The breakdown of the major minerals may liberate included accessory minerals into the reaction volume of the rock or alternatively may sequester these minerals away allowing their preservation when they would otherwise be consumed in a reaction sequence (e.g., Montel et al. 2000). Fourth, the microstructural relationships between accessory and major minerals provide context for delineating the *P–T* history of a metamorphic rock.

Garnet and plagioclase are the major minerals most commonly used in petrochronology because of their distinctive trace element behaviour. Linking their growth and breakdown to ages obtained from accessory mineral chronometers requires an understanding of the bulk composition controls on their stabilities. Below, we outline the controls on the growth and breakdown of garnet and plagioclase, which are of particular importance for petrochronology studies. Our focus is on linking mineral growth to metamorphic reactions and we do not discuss the minerals that are important for thermochronology studies (e.g., amphibole, biotite, muscovite, K-feldspar).

Garnet

Garnet is one of the most useful minerals for constraining metamorphic grade and its high density and strong partitioning of cations forms the basis of many useful thermobarometers (e.g., Spear 1995; Caddick and Kohn 2013). It is a common metamorphic mineral for many different protoliths (pelites, mafic rocks, ultramafic rocks, calc-silicates) and has been extensively used in petrochronology studies (e.g., Vance and O'Nions 1990; Vance and Mahar 1998; Harris et al. 2004). Coupling *P–T* estimates from garnet with monazite U–Pb geochronology can also be used to constrain *P–T–t* paths (e.g., Foster et al. 2000; Gibson et al. 2004; Dragovic et al. 2016). Garnet can also be directly dated using Sm–Nd and Lu–Hf geochronology (e.g., Baxter et al. 2013; Baxter et al. 2017, this volume). Although linking *P–T* information from garnet-bearing assemblages with garnet geochronology is very powerful (e.g., Mulcahy et al. 2014; Dragovic et al. 2012, 2015), direct dating of garnet is challenging and is not yet extensively used.

An important control on the stability of garnet during metamorphism is the bulk rock MnO content (e.g., Symmes and Ferry 1992; Mahar et al. 1997; White et al. 2014b). For pelites, higher bulk rock Mn concentrations stabilize garnet at lower temperatures in the greenschist facies and at lower pressure in the amphibolite facies (White et al. 2014b). The ratio of Fe/Mg is also an important control on garnet growth. For example, relatively magnesium-rich pelites have restricted garnet stability fields (e.g., White et al. 2014a) and in very Mg-rich bulk rock compositions garnet may not even grow along common *P–T* paths (e.g., Fitzsimons et al. 2005). Therefore, depending on the bulk composition of the rock, garnet can be first stabilized in the greenschist facies, the amphibolite facies or not at all.

Garnet is the most important major mineral sink for the heavy rare earth elements (HREE) and yttrium in metamorphic rocks (Bea et al. 1994). Accessory minerals such as zircon, monazite, xenotime, apatite, epidote and allanite are also important repositories for the HREE and Y. Thus, the growth and breakdown of garnet plays an important role in the HREE and Y budgets in rocks and links the trace element chemistry of accessory mineral chronometers to the *P–T* information obtained from garnet-bearing metamorphic assemblages (Pyle et al. 2001; Foster et al. 2002; Kohn et al. 2004; Rubatto 2002; Rubatto and Hermann 2007; Taylor et al. 2015). In general, the equilibrium distribution coefficients of the HREE between garnet and zircon are close to unity for Gd to Lu at high temperature (Taylor et al. 2015). For Yttrium, concentrations in monazite are ~1.5 orders of magnitude higher than in garnet (Bea et al. 1994). Xenotime has Y concentrations that are ~2 orders of magnitude higher than in monazite (Pyle et al. 2001). However, in most cases, garnet is substantially more modally abundant than monazite and xenotime and thus the breakdown or growth of garnet will exert first-order controls on the Y and HREE budget of the rock. Zircon and monazite crystallization during garnet growth will result in relatively low concentrations of HREE and Y in these minerals because these elements are partitioned into garnet. By contrast, garnet breakdown during accessory mineral growth can result in HREE- and Y-enriched trace element concentrations of the new growth zones of accessory minerals (e.g., Rubatto 2002; Foster et al. 2002, 2004).

Plagioclase

Plagioclase is extremely common in metamorphic rocks and is stable over a wide range of *P–T* conditions. Plagioclase breakdown with increasing pressure is an important part of the reaction sequences for high-pressure metamorphic rocks and eclogites. Similar to garnet, plagioclase is commonly a key mineral in thermobarometers that provides important *P–T* information in many different rock types (Ghent 1976; Wu 2015; Molina et al. 2015). For petrochronology, plagioclase (and to a lesser extent K-feldspar) strongly partitions Eu and Sr over the other major rock-forming minerals (e.g., Gromet and Silver 1983). The growth and breakdown of plagioclase can be tied to Eu anomalies in rare earth element patterns of accessory minerals (Rubatto et al. 2013; Holder et al. 2015; Regis et al. 2016). Strontium concentrations have been used to link accessory mineral growth to the timing of plagioclase breakdown; this is a particularity important relationship in ultrahigh pressure metamorphic rocks (Finger and Krenn 2007; Kylander-Clark et al. 2013; Holder et al. 2015).

ACCESSORY MINERALS

Like the major minerals, accessory minerals are involved in the reaction sequence experienced by metamorphic rocks. The behaviour of some accessory minerals used in petrochronology such as epidote, titanite and rutile can be quantified along a *P–T* evolution using phase equilibria modelling. However, the behaviour of zircon and monazite—the most commonly used mineral chronometers—is more difficult to quantify with current phase equilibria modelling techniques (e.g., Spear and Pyle 2010; Kelsey and Powell 2011) as they contain key elements commonly not considered in model chemical systems.

Epidote

Epidote is common in low–medium pressure metabasites, metamorphosed intermediate rocks and calc-silicates (e.g., Grapes and Hoskin 2004) as well as in high- to ultrahigh-pressure metamorphic rocks (e.g., Enami et al. 2004). The chemical controls on epidote stability are mainly bulk rock concentrations of Ca and Al as well as f_{O2} (e.g., Enami et al. 2004). The epidote-group minerals can be important repositories for Zr (e.g., Frei et al. 2004; Kohn et al. 2015) and LREE in metamorphic rocks (Frei et al. 2004; Janots et al. 2008). Therefore, the breakdown of Zr-rich epidote may have the potential to generate metamorphic zircon. Coupled allanite and epidote breakdown may produce new monazite (e.g., Janots et al. 2008) if there is also a source of phosphorus such as xenotime or apatite.

Titanite

Titanite is common in mafic rocks and in some low-grade metasedimentary rocks and it can be used as a barometer in metabasites (e.g., Kapp et al. 2009). An important factor in the stability of titanite is the relative activities of Ca and Al as influenced by the bulk rock ratio of Ca to Al and the accompanying mineral assemblage. High Ca activities favour titanite over ilmenite and high Al activities favour anorthite (and ilmenite) over titanite (Frost et al. 2001). Consequently, titanite is a common mineral in low-Al compositions such as calc-silicate and mafic rocks whereas aluminous metasedimentary rocks generally have ilmenite as the main Ti-bearing mineral above the greenschist facies.

Titanite can be directly dated using U–Pb geochronology, but there is some uncertainty about the closure temperature for Pb, which is generally considered to be around 600°C (Warren et al. 2012; Spencer et al. 2013; Stearns et al. 2015; Kirkland et al. 2016), depending on cooling rate. Diffusion profiles of trace elements in titanite can be used to determine the timing and duration of cooling (e.g., geospeedometry) and this is covered in more detail in Kohn (2017, this volume). Titanite thermometry uses the Zr concentration of titanite to estimate temperature (Hayden et al. 2008). However, application of this thermometer requires an estimate of titania activity (a_{TiO2}), which, in the absence of rutile, is difficult to constrain and can vary along a metamorphic evolution depending on the reaction sequences and mineral assemblages as discussed below.

Rutile

Rutile is commonly stable in relatively reduced bulk rock compositions (e.g., Diener and Powell 2010) and is particularity useful in high-pressure metamorphic rocks (Zack and Kooijman 2017). Similar to titanite, rutile can be directly dated with U–Pb geochronology (e.g., Mezger et al. 1989; Clark et al. 2000; Zack et al. 2011; Ewing et al. 2015) and it can be used as a geospeedometer (Smye and Stockli 2014). One of the main uses of rutile is as a thermometer that uses the Zr concentration of rutile to estimate temperature (Zack et al. 2004; Watson et al. 2006; Ferry and Watson 2007; Tomkins et al. 2007; Hofmann et al. 2013; Taylor-Jones and Powell 2015). These applications are discussed in more detail by Zack and Kooijman (2017, this volume).

Metamorphic reaction sequences with or without rutile have important implications for applying the Ti-in-quartz thermometer (e.g., Chambers and Kohn 2012; Ashley and Law 2015) and the Ti-in-zircon thermometer (e.g., Ferry and Watson 2007), both of which use a_{TiO2} as a variable. In rutile-bearing systems a_{TiO2} is buffered at 1.0. In rutile-absent systems, application of the thermometer requires an estimate of a_{TiO2} that is less that 1.0. Figure 1 shows the difference of calculated temperatures using the Ti-in-quartz thermometer (Wark and Watson 2006) and the Ti-in-zircon thermometer (Ferry and Watson 2007) as a function of temperature for a range of a_{TiO2} values.

For example, consider an amphibolite-facies rock at 650°C with a true a_{TiO2} value 0.6. If an a_{TiO2} value of 1.0 is assumed for Ti-in-quartz thermometry, the result would underestimate the true temperature by ~50°C (Fig. 1a). Similarly, using an a_{TiO2} value of 1.0 when the true value is 0.6, the Ti-in-zircon thermometer would underestimate the true temperature by ~40°C (Fig 1b). Phase equilibria modelling provides one method of determining a_{TiO2} in metamorphic rocks at different stages of a *P–T* evolution in rutile-absent rocks (e.g., Ashley and Law 2015). We explore this in more detail during our discussion of particular reaction sequences.

Zircon

Zircon is the main repository of Zr in most igneous and metamorphic rocks and is the most widely used accessory mineral for U–Pb geochronology (Hoskin and Schaltegger 2003; Rubatto 2017, this volume). Many metamorphic rocks contain relict zircon that may be detrital or igneous in origin and may also be inherited from a previous metamorphic event. For petrochronology, metamorphic zircon can be used to date different portions of a *P–T* evolution depending on the growth mechanisms. The main processes that increase the mode of zircon in metamorphic rocks include solid-state growth and the crystallization from anatectic melt. In some cases, zircon may precipitate from hydrothermal fluids (e.g., Schaltegger, 2007).

Solid-state zircon growth can occur from the breakdown of other Zr-rich minerals such as garnet (Fraser et al. 1997; Degeling et al. 2001), ilmenite (Bingen et al. 2001), rutile (Ewing et al. 2014) and possibly amphibole (Sláma et al. 2007). This zircon can be used to date major metamorphic assemblage changes during prograde (e.g., Fraser et al. 1997) or retrograde metamorphism (e.g., Degeling et al. 2001) depending on when the Zr-rich mineral breaks down during the reaction sequence. However, major minerals such as garnet, rutile and hornblende can accommodate more Zr as temperature increases and, in general, zircon will be consumed and prograde zircon growth is expected to be limited (Kohn et al. 2015).

The crystallization of anatectic melt typically drives new zircon growth in suprasolidus metamorphic rocks (Watson 1996; Roberts and Finger 1997; Schaltegger et al. 1999; Vavra et al. 1999; Hermann et al. 2001; Kelsey et al. 2008; Yakymchuk and Brown 2014b). Experimental studies show that the concentration of Zr in melt needed to maintain equilibrium with zircon increases with temperature (e.g., Harrison and Watson 1983; Gervasoni et al. 2016) and the compositional parameter M, which is the cation ratio of [Na + K + 2Ca]/ [Al x Si] (Watson and Harrison 1983; Boehnke et al. 2013). Generally, the concentration of Zr needed for saturation of intermediate melts (high M values) is higher than for more felsic melts (low M values). In suprasolidus metamorphic rocks, the most important factor is the amount of anatectic melt present in the system (Kelsey et al. 2008; Kelsey et al. 2011; Yakymchuk and Brown 2014b). As the fraction of melt increases during prograde metamorphism, zircon is expected to break down to maintain Zr saturation of the melt in an equilibrated system. Consequently, prograde zircon growth is expected to be limited above the solidus. In general, melt crystallization during cooling from peak *T* is expected to be the main mechanism for zircon growth in suprasolidus metamorphic rocks. This is supported by ranges of concordant ages that reflect protracted zircon growth during melt crystallization from peak *T* in migmatites (e.g., Korhonen et al. 2013b, 2014).

New zircon growth can also occur at the expense of pre-existing zircon with no change in the mode of zircon in the rock. Recrystallization of metamict zircon in the presence of a fluid may be an important factor for some prograde zircon (e.g., Rubatto and Hermann 2003; Hay and Dempster 2009). Ostwald ripening has been proposed as a mechanism that could produce prograde growth of zircon in suprasolidus metamorphic rocks (Vavra et al. 1999; Nemchin et al. 2001; Kawakami et al. 2013). Ostwald ripening (or second phase coarsening) is a process whereby small solids are preferentially dissolved and precipitate on existing larger solids to reduce the total surface free energy (e.g., Tikare and Cawley 1998). While this process has been studied and debated for the major minerals in metamorphic rocks (Miyazaki 1991, 1996; Carlson 1999, 2000) it has not been as extensively studied for accessory minerals—an exception being Nemchin et al. (2001). Nonetheless, it is a possible mechanism for prograde growth of zircon in suprasolidus metamorphic rocks, though involving no net modal increase in zircon.

Zircon can also be used as a thermometer in igneous and metamorphic rocks. The Ti-in-zircon thermometer has been increasingly applied to high-temperature metamorphic rocks over the last decade. Kelsey and Hand (2015) compiled Ti-in-zircon temperatures from UHT rocks and noted that 62% of the results fall below the UHT threshold of 900°C. One of the possible reasons for this discrepancy is that some UHT rocks do not contain rutile and are therefore undersaturated in TiO_2 ($a_{TiO2} < 1.0$). Values of a_{TiO2} can range from 1.0 when rutile is in equilibrium with growing zircon to values as low as 0.6 (e.g., Hiess et al. 2008). Using a value of

1.0 when rutile is absent will underestimate the true temperature. Again, the presence and absence of rutile during a reaction sequence has important consequences for applying mineral thermometers in metamorphic rocks.

Monazite

Monazite is generally more reactive than zircon in subsolidus metamorphic rocks and has been extensively used for U–Pb geochronology in aluminous bulk compositions (e.g., Parrish 1990; Engi 2017, this volume). Monazite can be detrital in origin (Smith and Barreiro 1990; Kingsbury et al. 1993; Suzuki et al. 1994; Rubatto et al. 2001), produced through solid-state reactions (e.g., Rubatto et al. 2001; Wing et al. 2003), precipitated from a fluid (e.g., Ayers et al. 1999) or can crystallize from anatectic melt (e.g., Stepanov et al. 2012).

Solid-state monazite growth during prograde metamorphism occurs from the breakdown of LREE-rich precursors, which can include: allanite for high-Ca bulk compositions (Spear and Pyle 2010; Wing et al. 2003; Finger et al. 2016), LREE-rich clays (Copeland et al. 1971), Th or LREE oxides and hydrous phosphates (Spear and Pyle 2002). The most studied solid-state reaction is the growth of monazite at the expense of allanite in bulk compositions with sufficient Ca and LREE to grow allanite at lower grade (e.g., Janots et al. 2008). In natural examples, this reaction has been spatially correlated with the garnet-in isograd (Catlos et al. 2001; Foster et al. 2004), the staurolite-in isograd (Smith and Barriero 1990; Kohn and Malloy 2004; Corrie and Kohn 2008) and the kyanite or sillimanite-in isograds (Wing et al. 2003; Štípská et al. 2015).

Spear (2010) used phase equilibria modelling to examine the *P*–*T* conditions of the allanite to monazite transition in several bulk rock compositions relative to the average pelite of Shaw (1956). The reaction boundaries for monazite-in at the expense of allanite for these various compositions are summarized in Figure 2. A higher bulk rock CaO concentration allows allanite to persist to higher temperatures whereas a higher Al_2O_3 concentration stabilizes monazite at lower temperatures. However, the results of this modelling of monazite growth in rocks with variable bulk rock Al_2O_3 concentrations by Spear (2010) are different to those observed in some natural examples. For example, Wing et al. (2003) found that pelites from New England with relatively elevated Ca and/or Al concentrations can preserve allanite to higher temperatures. Gasser et al. (2012) found no link between bulk rock concentrations of CaO and Al_2O_3 and the timing of monazite growth. Therefore, the bulk compositional controls of monazite growth at the expense of allanite are not always clear, but it appears that monazite can grow at a range of temperatures and pressures along a prograde *P–T* path.

The relative amounts of iron and magnesium in a bulk rock composition may also play an important role in the reactions that produce subsolidus monazite. For example, Fitzsimons et al. (2005) showed that monazite in pelitic schists from Western Australia was generated during garnet-breakdown to staurolite and was interpreted to record the timing of peak metamorphism. However, samples that were too magnesium-rich to grow garnet or too iron-rich to grow staurolite at the expense of garnet yielded older monazite ages. Fitzsimons et al. (2005) interpreted these older ages to represent greenschist-facies monazite growth.

In suprasolidus metamorphic rocks, monazite breakdown and growth is controlled mainly by dissolution into and crystallization from anatectic melt. Experimental studies demonstrate that monazite dissolution into melt is a function of temperature, pressure, and the bulk composition of the melt (Montel 1986; Rapp and Watson 1986; Rapp et al. 1987; Skora and Blundy 2012; Stepanov et al. 2012; Duc-Tin and Keppler 2015). The solubility of monazite increases with higher H_2O concentrations in melt (Stepanov et al. 2012) and with decreasing phosphorus concentrations in the melt (Duc-Tin and Keppler 2015). Studies that couple experimentally-determined solubility equations of monazite with phase equilibria modelling show that monazite dissolution increases during prograde metamorphism above the solidus and that for UHT metamorphism most monazite will be completely consumed along the prograde path (Kelsey et al. 2008; Yakymchuk and Brown 2014b). Based on these theoretical models of monazite behaviour, no prograde monazite growth is expected above the solidus. This contrasts with studies of natural rocks that record prograde suprasolidus monazite growth (e.g., Hermann and Rubatto 2003; Hacker et al. 2015). Johnson et al. (2015) suggest that apatite dissolution during prograde metamorphism may have contributed to LREE saturation of the melt and resulted in prograde suprasolidus monazite crystallization. However, the role of apatite breakdown and monazite growth in suprasolidus metamorphic rocks is still poorly understood.

Finally, similar to zircon, Ostwald ripening could produce prograde monazite growth in suprasolidus metamorphic rocks (e.g., Nemchin and Bodorkos 2000). However, this has not been extensively studied and may only apply to monazite growth just above the solidus where the modal proportion of anatectic melt is relatively low.

Xenotime

Xenotime is a common phosphate in low- to high-grade metamorphic rocks (e.g., Franz et al. 1996; Bea and Montero 1999; Pyle and Spear 1999; Spear and Pyle 2002). It can be directly dated using U–Pb geochronology (e.g., Parrish 1990; Rasmussen et al. 2005, 2007, Sheppard et al. 2007; Janots et al. 2009; Crowley et al. 2009) and can be used as a thermometer when in equilibrium with monazite and garnet (Pyle et al. 2001). Some of the proposed mechanisms of metamorphic xenotime growth are: (1) growth due to dissolution/reprecipitation of detrital or diagenetic zircon (Dawson et al. 2003; Rasmussen et al. 2011), (2) growth during to the breakdown of detrital zircon (Franz et al. 2015), (3) growth during the breakdown of allanite and/or monazite (Janots et al. 2008), (4) crystallization from anatectic melt (Pyle and Spear 1999; Crowley et al. 2009), and (5) growth during the breakdown of Y-rich garnet (e.g., Pyle and Spear 1999).

There are three important controls on the stability of xenotime in metamorphic rocks. First, higher bulk rock Yttrium concentrations allow xenotime to persist to higher pressures and temperatures (Spear and Pyle 2010). Second, similar to monazite and zircon, partial melting will result in xenotime consumption in order to contribute to REE and P saturation of the melt (e.g., Wolf and London 1995; Duc-Tin and Keppler 2015). Third, xenotime will be consumed during the growth of garnet, which partitions Y and HREE (Pyle and Spear 1999, 2000; Spear and Pyle 2002). Consequently, xenotime in the matrix of high-grade garnet-bearing rocks is relatively rare although xenotime inclusions may be present in garnet (e.g., Pyle and Spear 1999). By contrast, xenotime may be present in the matrix at various metamorphic grades in garnet-absent rocks.

PHASE EQUILIBRIA MODELLING

Phase assemblages in metamorphic rocks generally change through continuous or multivariant reactions rather than discontinuous or univariant reactions (e.g., Stüwe and Powell 1995; Kelsey and Hand 2015). Petrogenetic grids display discontinuous reactions and may yield the false impression that reactions occur over narrow intervals along a *P*–*T* path (e.g., Vernon 1996). In reality, mineral (and melt) modes and compositions are continuously changing along a *P*–*T* evolution and these variations represent the reaction sequence of the rock. The particular reaction sequence experienced by a metamorphic rock is dependent on bulk composition, the *P*–

T path and whether the system is open or closed (e.g., White and Powell 2002; Brown and Korhonen 2009; Yakymchuk and Brown 2014a). The phase assemblages expected for a particular bulk rock composition over a range of *P*–*T* conditions are commonly depicted using *P*–*T* pseudosections, phase diagrams constructed for a fixed bulk composition (e.g., Hensen 1971; Worley et al. 1998; Spear et al. 2016). More detailed information about the reaction sequences can be determined by using the intersection of a *P*–*T* path with isopleths (or contours) of different variables (e.g., mineral modes and compositions) on a pseudosection or by constructing mode–temperature or mode–pressure diagrams (e.g., White et al. 2011).

Here, we present pseudosections and mode-box diagrams (*P*/*T*–mode plots) for different bulk chemical compositions to investigate the reaction sequences along common *P*–*T* paths and we discuss the consequences for interpreting the ages obtained from accessory mineral geochronology. The effects of fractionation of growing porphyroblasts and changes in bulk composition are discussed later. Because we use phase equilibria modelling, it is assumed that there are no kinetic controls (e.g., nucleation barriers or sluggish diffusion) that impact the growth or dissolution of major and accessory minerals. Although this assumption may not be strictly valid in some circumstances (Watt and Harley 1993; Pattison and Tinkham 2009; Gaides et al. 2011; Pattison and Debuhr 2015), the modelling here provides a general framework for investigating reaction sequences.

Bulk compositions

Three bulk chemical compositions are modelled that represent the most common protoliths investigated during most metamorphic studies. For the subsolidus and suprasolidus *P*–*T* paths, this includes an average amphibolite-facies metapelite (Ague 1991) and an average passive margin greywacke (Yakymchuk and Brown 2014a). These two compositions were chosen because they are expected to dominate passive margin turbidite sequences that are involved in orogenesis at convergent plate boundaries. A mid-ocean ridge basalt (MORB) from Sun and McDonough (1989) was also used to investigate a suprasolidus reaction sequence for a typical mafic protolith. The modelled bulk compositions are summarized in Table 1. Note that we do not consider melt loss nor fractionation of minerals away from the reacting volume in the modelling here, both of which can modify the composition of the equilibrium volume during a metamorphic evolution (e.g., White and Powell 2002; Evans 2004; Guevara and Caddick 2016; Mayne et al. 2016).

Computational Methods

Forward phase equilibria modelling is used to evaluate the changes to metamorphic mineral assemblages along several schematic *P*–*T* paths. There are two main approaches to phase equilibria modelling. The first approach is to use Gibbs free energy minimization to determine the stable mineral assemblage at a given *P*–*T* condition and there are two commonly used software packages available for this approach, including Perple_X (Connolly and Petrini 2002) and Theriak–Domino (de Capitani and Brown 1987; de Capitani and Petrakakis 2010). A second approach is to determine the solution of simultaneous non-linear equations to build up an array of points and lines that make up a metamorphic phase diagram (THERMOCALC: Powell and Holland 1988; Powell et al. 1998; Powell and Holland 2008). Both of these approaches require an internally consistent thermodynamic database derived from the results of experimental studies. There are several commonly-used databases available: Berman (1988), Holland and Powell (1998) and most recently Holland and Powell (2011). Finally, the calculations require activity–composition models that relate end-member proportions to end-member activities for the solid-solution minerals as well as for complex fluids and melt.

Here, calculations were performed using THERMOCALC v.3.40 (Powell and Holland 1988) using the internally consistent dataset of Holland and Powell (2011). For metapelite and greywacke compositions, modelling was undertaken in the MnO–Na_2O–CaO–K_2O–FeO–MgO–Al_2O_3–SiO_2–H_2O–TiO_2–Fe_2O_3 (MnNCKFMASHTO) chemical system using the activity–composition relations in White et al. (2014a,b). An average MORB composition was investigated in the NCKFMASHTO chemical system using the activity-composition models from Green et al. (2016). Phases modelled as pure end-members are quartz, rutile, titanite, aqueous fluid (H_2O), kyanite and sillimanite. Mineral abbreviations are from Holland and Powell (2011) with the exception of titanite (ttn).

Phase equilibria modelling of subsolidus and suprasolidus systems requires different approaches to approximate the bulk H_2O content of the system. For subsolidus phase equilibria modelling, the amount of H_2O in each bulk composition was set to be in excess, such that $a_{H2O} =1$. By contrast, suprasolidus rocks are generally not considered to have excess H_2O as the very small amount of free H_2O at the solidus is partitioned into anatectic melt (Huang and Wyllie 1973; Thompson 1982; Clemens and Vielzeuf 1987; White and Powell 2002; White et al. 2005). Along the solidus, the solubility of H_2O in anatectic melt increases with pressure. Therefore, for phase equilibria modelling of suprasolidus rocks, the amount of H_2O in the bulk composition must be set, and was adjusted so that the melt is just saturated with H_2O at solidus at 8 kbar. If the modelled prograde path crossed the solidus at lower or higher pressures, the quantity of melt produced will be slightly overestimated and underestimated, respectively.

Modelled *P–T* paths

Several simplified typical *P–T* paths for subsolidus and suprasolidus systems are modelled to investigate the reaction sequences, changes in mineral modes, amount of melt generated and/or consumed, variations in bulk rock a_{TiO2} and the consequences for interpreting the results of accessory mineral geochronology. Two subsolidus and two suprasolidus *P–T* paths were investigated for the metapelite and greywacke compositions that represent different tectonic evolutions. We also model one suprasolidus *P–T* path for a MORB composition applicable to high-pressure mafic granulites.

For the subsolidus systems, the first *P–T* path has a clockwise trajectory and is representative of collisional orogenesis (e.g., England and Thompson 1984; Thompson and England 1984). An important feature of this *P–T* path is that peak *P* occurs before peak *T*, which is consistent with a relatively long residence time in the core of an orogenic belt. The model path (‘clockwise’ in Figs 3, 5) contains four segments: (1) heating and burial up to 10 kbar and 550°C, (2) isobaric heating up to 650°C, (3) decompression and minor heating to 8 kbar and 660°C, and (4) decompression and cooling to 6.2 kbar and 610°C.

The second subsolidus *P–T* path has a ‘hairpin’ trajectory where peak *P* and peak *T* nearly coincide (e.g., ‘hairpin’ in Figs 3, 5). This style of *P–T* path is also common in collisional orogenesis (e.g., Brown 1998; Kohn 2008) and reflects relatively short residence times at depth and can represent crustal thickening in an accretionary zone of a propagating orogen (Jamieson et al. 2004). The model hairpin *P–T* path contains three segments: (1) heating and burial up to 7 kbar and 610°C, (2) heating and decompression to 6 kbar and 650°C, and (3) decompression and cooling to 4 kbar and 600°C. Peak metamorphism is at the same temperature for both subsolidus *P–T* paths, but the pressures at peak *T* are different.

Two *P–T* paths for suprasolidus rocks that are typical of granulite-facies metamorphism are investigated. First, a clockwise *P–T* path is modelled (e.g., ‘clockwise’ in Figs 7, 9) that is associated with crustal thickening and heating and is typical of many granulite terranes (e.g., Clark et al. 2011). This *P–T* path contains four segments: (1) increase in pressure and heating across the solidus up to 9 kbar at 850°C, (2) isobaric heating up to 900°C, (3) isothermal decompression to 7 kbar, and (4) cooling and decompression to 5 kbar at 750°C.

Second, a suprasolidus counterclockwise (or anticlockwise) *P–T* path is considered (e.g., ‘counterclockwise’ in Figs 7, 9) and is common in high temperature–low pressure terranes (e.g., Clarke et al. 1987; Collins and Vernon 1991) and some ultrahigh temperature terrains (e.g., Korhonen et al. 2013a, 2014). This *P–T* path reflects heating prior to thickening (usually at peak *T*) followed by near-isobaric cooling. In some cases, this has been attributed to the inversion of a hot back-arc basin during collisional orogenesis (Clark et al. 2014). The modelled counterclockwise *P–T* path contains four segments: (1) isobaric heating up to 830°C and 5 kbar, (2) heating and an increase in pressure up to 860°C and 6 kbar, (3) cooling and an increase in pressure to 850°C and 7 kbar, and (4) isobaric cooling to 750°C.

A high-pressure clockwise path was also chosen to model the reaction sequences for high-pressure mafic granulites (e.g., O’Brien and Rötzler 2003) and to investigate the growth and breakdown of garnet for these rocks. This *P–T* path contains four segments: (1) heating and an increase in pressure up to 12 kbar and 850°C, (2) isobaric heating up to 950°C, (3) isothermal decompression to 8 kbar, and (4) cooling and decompression to 800°C and 6 kbar. The decompression segments of this *P–T* path are also compatible with the decompression segments of some ultrahigh-pressure metamorphic rocks (Hacker et al. 2010; Chen et al 2013; Xu et al 2013).

Modelling suprasolidus zircon and monazite dissolution

For the suprasolidus *P–T* paths, the growth and dissolution of zircon and monazite are modelled using the method of Kelsey et al. (2008). Note that the bulk composition used in this modelling is fixed without fractionation of elements into growing porphyroblasts (e.g., zirconium into garnet) or loss of melt. These factors are discussed later. First, the saturation concentrations of the melt in ppm are calculated as follows. The major element composition of the anatectic melt is calculated at a specified *P–T*. This composition of the melt is combined with the solubility equations of Boehnke et al. (2013) for zircon and Stepanov et al. (2012) for monazite, and the stoichiometric concentrations of Zr in zircon (497,664 ppm Zr) and LREE in monazite (566,794 ppm LREE) to determine the saturation concentrations of Zr and LREE in ppm (Kelsey et al. 2008). These initial calculations do not account for the proportion of anatectic melt or the bulk-rock concentrations of Zr and LREE. Second, the saturation concentrations of Zr or LREE (ppm) are multiplied by the proportion of anatectic melt in the system (in normalized mol% which is approximately equivalent to vol%) at *P–T* to arrive at concentrations in ppm that are required to saturate the melt in the equilibration volume of the rock. Finally, these values are divided by the assumed bulk-rock chemical concentrations of Zr and LREE. The Zr and LREE in pelites and the greywackes are generally similar to each other and to the values of metasedimentary migmatites; a value of 150 ppm was chosen here (e.g., Yakymchuk and Brown 2014b). For MORB, the Zr concentration was set at 103 ppm, which is an average of global MORB compositions (White and Klein 2014). The sensitivity of these calculations to bulk rock concentrations of Zr and LREE and the assumptions and limitations of this methodology are discussed by Kelsey et al. (2008) and Yakymchuk and Brown (2014b). The result of the calculations is the proportion of zircon or monazite dissolution required to saturate the anatectic melt in Zr and LREE in the equilibration volume of the rock. This value is subtracted from 100% and the results are reported as the percent of zircon and monazite remaining relative to the amounts existing at the fluid-present solidus for each *P–T* path.

One important limitation of the monazite saturation equation used here is that it does not account for phosphorus in anatectic melt, which can affect monazite stability (e.g., Duc-Tin and Keppler 2015). The main repository of phosphorus in most metamorphic rocks is apatite, which is expected to break down during partial melting (Wolf and London 1994). Phosphorus saturation in melt is a function of temperature, SiO_2 concentration (Harrison and Watson 1984) and the aluminum saturation index of the melt (ASI = molar [Al_2O_3] / [K_2O + Na_2O + CaO], Wolf and London 1994). The solubility of apatite in melt increases with rising ASI, which is common during prograde partial melting in migmatites (e.g., Johnson et al. 2015). For example, an increase in the ASI from 1.1 to 1.2 increases the solubility of apatite by an order of magnitude (Wolf and London 1994). The breakdown of LREE-rich apatite during prograde metamorphism may contribute to LREE saturation of anatectic melt and monazite crystallization (e.g., Johnson et al. 2015; Rocha et al. 2016). Here, we use melt ASI as a qualitative tool to investigate the behaviour of apatite during partial melting and the consequences for prograde monazite growth in suprasolidus metamorphic rocks.

SUBSOLIDUS PHASE RELATIONS AND REACTION SEQUENCES

Phase relations and reaction sequences for two subsolidus *P–T* paths for two bulk compositions are discussed below for a closed system where bulk composition does not change. Fractionation of porphyroblasts away from the reacting volume is not considered in the calculations here.

Metapelite

Phase relations. The pseudosection for the amphibolite-facies metapelite is shown in Figure 3. Biotite is stable at $T > 450$–460°C with increasing pressure. Garnet is stable across most of the diagram except at low P and low T and at $P < 5$ kbar just below the solidus. The staurolite-in field boundary extends from 550°C at 4 kbar up to 650°C at 10 kbar. The stability field of the aluminosilicate minerals (kyanite and sillimanite) ranges from $T > 580$°C at 4 kbar to $T > 660$°C at 10 kbar. Rutile is stable at low P at low temperatures and at $P > 10.5$ at $T > 550$°C.

Reaction sequence for the clockwise P–T path. A mode-box for the reaction sequence for the clockwise P–T path is shown in Figure 4a. During the prograde segment of the clockwise P–T path, chlorite is progressively consumed to produce biotite (starting at 455°C) and then garnet (starting at 460°C). Chlorite is exhausted by 580°C. Rutile is completely consumed by ~530°C. Epidote breaks down along the prograde path and the epidote-out field boundary is encountered at 620°C. The complete breakdown of epidote at 620°C may result in minor zircon crystallization or more likely the growth of new rims on pre-existing zircon.

The staurolite stability field is encountered during the heating and decompression segment at 9 kbar and 650°C. In natural examples, prograde monazite growth has been associated with garnet, staurolite and kyanite/sillimanite growth in metapelites (Catlos et al. 2001; Smith and Barriero 1990; Wing et al. 2003; Kohn and Malloy 2004; Fitzsimons et al. 2005; Corrie and Kohn 2008), although kyanite/sillimanite is not encountered along the P–T path modelled here. In general, monazite could grow at different points along the prograde P–T path. Because garnet growth is predicted to be continuous up to the staurolite-in field boundary, new monazite grown during this segment of the *P–T* path is expected to have low concentrations of HREE and Y; these elements are expected to partition into garnet. Staurolite growth is at the expense of garnet and occurs during the decompression portion of the prograde path (e.g., Florence and Spear 1993). Monazite formed during this segment is expected to have elevated HREE and Y concentrations due to the breakdown of garnet and the age would record the initial stages of decompression from peak *P*. By contrast, zircon is expected to undergo only minor changes to its mode and will be slightly consumed during subsolidus prograde metamorphism (e.g., Kohn et al. 2015). Two possible exceptions are minor zircon growth during the breakdown of Zr-rich epidote and/or rutile. However, at low temperatures, rutile is not expected to be zirconium rich.

The stable mineral assemblage at the metamorphic peak of 660°C and 8 kbar includes garnet, staurolite, biotite, plagioclase, ilmenite, muscovite and quartz. In general, the mode of monazite in metapelites is expected to reach a maximum at peak *P–T* and monazite is not expected to grow during cooling (e.g., Spear and Pyle 2010). An additional factor is that monazite is susceptible to dissolution/reprecipitation in the presence of fluids (e.g., Williams et al. 2011). While fluid-mediated dissolution/reprecipitation should not increase the net mode of monazite, it can occur at almost any point along the *P–T* evolution. Therefore, it is possible that monazite in a subsolidus metapelite can record a range of ages that vary from monazite-in up to the metamorphic peak and dissolution/precipitation may result in ages that record retrogression (Harlov et al. 2005; Williams et al. 2011). On the other hand, zircon is expected to be relatively unreactive and may not record prograde to peak metamorphism in subsolidus metamorphic rocks.

After the exhaustion of rutile during the heating and burial segment the value of a_{TiO2} decreases to 0.95 initially and remains nearly constant until the decompression and heating segment, where a_{TiO2} drops to 0.8. During the subsequent decompression and cooling segment the a_{TiO2} value remains stable at 0.8. After rutile is exhausted, any growth of new zircon or modification of existing zircon will occur when $a_{TiO2} < 1.0$; this needs to be considered when applying the Ti-in-zircon thermometer.

Reaction sequence for the hairpin P–T path. A mode-box for the reaction sequence for the hairpin *P–T* path is shown in Figure 4b. The prograde reaction sequence includes garnet-in at 520°C and 4.5 kbar, staurolite-in at 590°C and 6.5 kbar and sillimanite-in at 640°C and 6 kbar. Garnet both grows and is consumed during the prograde portion of the reaction sequence. The value of a_{TiO2} decreases from 0.88 at 500°C to 0.79 at peak *T*. For the decompression and cooling segment, a small amount of biotite grows at the expense of garnet; the modes of the other minerals are little changed and the a_{TiO2} value remains close to 0.79.

As with the clockwise *P–T* path, monazite growth may occur at various times during the prograde segment of the hairpin *P–T* path. Because the mode of garnet increases and decreases multiple times during the prograde reaction sequence, linking Y and HREE in monazite would be challenging in the absence of microstructural context, such as monazite in coronae surrounding resorbed garnet. For example, HREE and Y-rich monazite could be generated during: (1) the heating and burial segment during garnet breakdown to staurolite, (2) the heating and decompression segment during garnet breakdown to biotite near the metamorphic peak, or (3) garnet breakdown during the retrograde segment of the *P–T* path. Furthermore, xenotime breakdown during prograde metamorphism would also contribute to the growth of Y and HREE-rich monazite with or without a contribution from garnet (e.g., Spear and Pyle 2010). Therefore, for the hairpin *P*–*T* path modelled here, HREE- or Y-rich monazite can record burial and/or exhumation.

Greywacke

Phase relations. The pseudosection for the greywacke is shown in Figure 5. Garnet is stable across the entire diagram. Titanite is stable at $T < 460$–470°C with increasing pressure. Biotite is stable across the diagram except at the high-*P*–low-*T* corner. Chlorite is unstable above 600°C at 7 kbar and unstable above 530°C at 12 kbar. Albite is stable below 565°C at 4 kbar and below 620°C at 11 kbar. White mica (muscovite and/or paragonite) is stable up to the solidus at $P > 10$ kbar and at $T < 570$°C at 4 kbar. There are two important sets of quasi-linear field boundaries with positive slopes in *P*–*T* space. First is the set of boundaries that range from 480°C at 4 kbar up to 640°C at 12 kbar represent the breakdown of epidote to produce plagioclase. A second set of fields extends from 570°C at 4 kbar to the solidus with increasing *P* that represent the consumption of paragonite to produce sillimanite or kyanite.

Reaction sequence for the clockwise P–T path. A mode-box for the assemblage sequence for the clockwise *P*–*T* path is shown in Figure 6a. For the clockwise *P*–*T* path the important changes along the prograde reaction sequence include: (1) the growth of rutile commencing at 460°C resulting in a_{TiO2} increasing from 0.9 at 450°C to 1.0 at 460°C, (2) the complete consumption of titanite by 475°C, (3) the growth of biotite and garnet at the expense of chlorite and muscovite from 450°C to 550°C, which results in the complete consumption of chlorite by 550°C, (4) the breakdown of epidote to produce 2 mol% plagioclase at ~605°C, (5) the consumption of ~0.5 mol% garnet to produce plagioclase and hematite from 605°C to 620°C, and (6) the growth of 0.5 mol% garnet from 620°C to 650°C. Similar to the metapelite, the breakdown of Zr-rich epidote may result in minor zircon growth.

Decompression and heating from 10 kbar at 650°C to 8 kbar at 660°C results in: (1) the disappearance of rutile at 9.8 kbar and a subsequent drop in a_{TiO2}, and (2) the breakdown of paragonite and garnet to produce kyanite, biotite and plagioclase at 8.8 kbar. The peak metamorphic assemblage at 660°C and 8 kbar includes garnet, kyanite, muscovite, biotite, plagioclase and ilmenite. Further decompression and cooling results in the growth of biotite at the expense of garnet and a gradual decrease in a_{TiO2}.

Like the metapelite, garnet breakdown occurs during a portion of the heating and burial segment of the *P–T* path (at ~600°C) and during the heating and decompression segment immediately before the metamorphic peak. Therefore, Y- and HREE-rich monazite associated with garnet breakdown could record the timing of burial and/or exhumation.

Reaction sequence for the hairpin P–T path. A mode-box for the reaction sequence for the hairpin *P–T* path is shown in Figure 6b. The hairpin *P–T* path has three notable differences in its reaction sequence compared with the clockwise path for the greywacke. First, the *P–T* path does not intersect the epidote stability field. Second, the value of a_{TiO2} is always less than one and decreases from 0.95 to 0.80 along the *P–T* path. And third, white mica is completely consumed by the end of the *P–T* path. In contrast to the multiple garnet growth/consumption segments along the clockwise *P–T* path, the mode of garnet increases during burial and decreases during decompression for the hairpin path. Therefore, Y- and HREE-depleted monazite is predicted to record burial and monazite enriched in these elements would document garnet-breakdown during decompression and/or cooling and may also record xenotime breakdown.

SUPRASOLIDUS PHASE RELATIONS AND REACTION SEQUENCES

Phase relations and reaction sequences for three suprasolidus scenarios are discussed below for a closed system where bulk composition does not change and the water content is fixed to just saturate the rock in H_2O at 8 kbar at the solidus. This approach provides important first-order constraints on the reaction sequences for the modelled compositions; it does not take into account melt loss and the associated effects on rock fertility, solidus temperature and zircon and monazite stability. The consequences of open system behaviour on the reaction sequence and accessory mineral stability are discussed later.

Metapelite

Phase Relations. The pseudosection for the metapelite is shown in Figure 7. Ilmenite and plagioclase are stable across the entire diagram. Garnet is stable at high pressures across the diagram except at $T < 700$°C at $P < 5.5$ kbar. Cordierite is stable at high-*T*–low-*P* conditions. Orthopyroxene is not stable in this diagram. Rutile is restricted to $P > 10$–11.5 kbar across the modelled temperature range. The three important partial melting reactions for the metapelite include: (1) the consumption of any free aqueous fluid to produce melt at the wet solidus, which ranges from 660°C at low pressures to 710°C at high pressure, (2) the incongruent breakdown of muscovite to produce K-feldspar, which is represented by a narrow low-variance field that extends from the wet solidus at low *P* to $T > 780$°C at $P > 12$ kbar, and (3) the progressive breakdown of biotite at temperatures above the muscovite stability field to produce either garnet at higher pressure or cordierite ± garnet at lower pressure. Biotite is exhausted by 850°C at $P > 7$ kbar and melting progresses via the consumption of quartz and feldspar.

Reaction sequence for the clockwise P–T path. The mode-box and titania activity for the clockwise assemblage sequence are shown in Figure 8a. The predicted amount of monazite and zircon remaining as well as melt ASI are shown in Figure 8b. During the prograde segment of the clockwise *P–T* path, the metapelite begins to melt at the wet solidus at ~680°C through the consumption of any free H_2O as well as quartz and plagioclase. The amount of aqueous fluid at the solidus is expected to be small given the limited porosity of high-grade metamorphic rocks (e.g., Yardley and Valley 1997). Therefore, the amount of melt produced at the wet solidus is expected to be limited. For the modelled metapelite, the amount of melt produced is 4 mol%, although this is mostly an artefact of the modelling which assumes H_2O saturation of the solidus at 8 kbar.

After any free H_2O is consumed, partial melting continues with increasing temperature through the consumption of muscovite up until 728°C. This produces an additional 3 mol% melt with a generally constant melt ASI. At 728°C and 7.5 kbar, melting proceeds via the incongruent breakdown of muscovite to generate K-feldspar over a narrow (~2°C) temperature range. This narrow field produces an additional 3 mol% melt. After muscovite is exhausted, the rock contains ~9 mol% melt and approximately 8% of the zircon and 12% of the monazite that was present at the solidus is predicted to have been consumed. A minor amount of apatite breakdown is expected in order to saturate the anatectic melt in phosphorus.

After muscovite is completely consumed, partial melting continues through the consumption of biotite, plagioclase and quartz to produce melt, garnet, K-feldspar and ilmenite.

This produces an additional 32 mol% melt. Because biotite is an important host of accessory mineral inclusions (e.g., Watson et al. 1989), biotite breakdown may release inclusions of monazite and zircon into the reaction volume of the rock. The liberation of these accessory minerals may contribute to LREE and Zr saturation of the anatectic melt. On the other hand, some zircon and monazite may be included in growing garnet and will be sequestered away from the reaction volume. These minerals will be shielded from dissolution and are more likely to preserve inherited (or detrital) ages as well as any subsolidus to early suprasolidus prograde metamorphic ages. The inclusion of accessory minerals in major minerals effectively reduces the Zr and LREE available to the system and proportionally more zircon and monazite dissolution will be required to maintain melt saturation in these elements (e.g., Yakymchuk and Brown 2014b). Therefore, the sequestration of zircon and monazite in stable peritectic minerals such as garnet will promote the dissolution of accessory minerals along grain boundaries in the matrix of the rock with increasing *T*.

Titania activity is predicted to reach its highest value of 0.92 at 850°C. At this point, all of the monazite and 85% of the zircon are expected to be consumed. However, during this interval, the ASI of the melt increases from 1.10 to 1.15, which may result in enhanced apatite dissolution. For example, Pichavant et al. (1992) estimate that a similar increase in ASI at 800°C and 5 kbar would change the P_2O_5 concentration of melt from 0.50 to 0.75 wt%. If apatite is LREE rich, the dissolution of apatite may delay the complete dissolution of monazite to higher temperatures or, in extreme cases, may even promote prograde monazite crystallization (e.g., Johnson et al. 2015).

After the complete consumption of biotite, the hydrous minerals have been exhausted and the residuum is essentially composed of anhydrous minerals. Melting continues through the continued consumption of quartz and K-feldspar up to the modelled peak temperature of 900°C. The ASI of the melt reaches 1.18 at peak *T* and significant apatite dissolution is likely. At this point, the metapelite contains 43 mol% melt and both monazite and zircon are absent. After zircon and monazite are completely consumed, further anatexis is expected to generate melt that is undersaturated in Zr and LREE. Therefore, even with the breakdown of LREE-rich apatite, prograde monazite crystallization is not expected above ~850°C.

Isothermal decompression from 9 to 7 kbar produces an additional 11 mol% melt at the expense of quartz and K-feldspar. At this point the rock contains the maximum amount of melt of 54 mol%. During this decompression segment, melt ASI increases from 1.18 to 1.23 and a_{TiO2} decreases from 0.86 to 0.74. Approximately 1 mol% garnet is consumed during decompression, which would liberate some HREE and Y into the reaction volume. If significant apatite dissolution occurs and promotes monazite crystallization during decompression, this may be reflected as elevated HREE concentrations in monazite. However, the melt is undersaturated in LREE given the complete exhaustion of monazite at 850°C so new monazite growth is unlikely unless the apatite is very enriched in LREE or the modal proportion of apatite is high.

Decompression and cooling from peak *T* results in: (1) melt crystallization, (2) the growth of K-feldspar and quartz until the cordierite stability field is reached at ~880°C and 6.7 kbar, (3) garnet and cordierite consumption to produce biotite, (4) new zircon and monazite growth, (5) a decrease in melt ASI and a_{TiO2}. Melt crystallization and cordierite growth are concomitant with the consumption of garnet and sillimanite; this is a common reaction sequence for high-temperature decompression in migmatites. Zircon or monazite produced over this reaction interval is expected to be enriched in HREE and Y (e.g., Yakymchuk et al. 2015). Protracted monazite and zircon growth will occur from peak *T* to the solidus. U–Pb zircon and monazite ages that spread down Concordia have been interpreted to record protracted growth during cooling and melt crystallization in various migmatite terranes with clockwise *P–T* evolutions (Korhonen et al. 2012; Reno et al. 2012; Morrisey et al. 2014; Walsh et al. 2015).

Reaction sequence for the counterclockwise P–T path. The mode-box and titania activity for the counterclockwise assemblage sequence are shown in Figure 8c. The amount of monazite and zircon remaining as well as melt ASI are shown in Figure 8d. During isobaric heating at 5 kbar, partial melting begins at the wet solidus at ~670°C and continues through the breakdown of muscovite to produce a total 8 mol% melt by 685°C. Melting continues via the progressive breakdown of biotite to produce peritectic garnet and K-feldspar. By 765°C, 17 mol% melt is present and roughly 80% and 60% of the initial amount of zircon and monazite, respectively, remains. From the solidus up to 765°C, the a_{TiO2} value of the system has decreased from 0.9 to 0.6 and the ASI of the melt has increased from 1.13 to 1.18. An increase in melt ASI increases the solubility of apatite; this may liberate some LREE and P that could contribute to minor monazite crystallization because the melt is predicted to be saturated with respect to the LREE. Similar to the clockwise *P–T* path, the breakdown of biotite may liberate zircon and/or monazite that was sequestered away from the reacting volume.

Cordierite enters the phase assemblage at ~770°C and melting continues through the breakdown of biotite, sillimanite and plagioclase to produce K-feldspar, garnet and cordierite. Sillimanite is completely consumed by 780°C and biotite is exhausted by 800°C. During the interval from 770°C to 800°C, approximately 15 mol% melt is generated and melt ASI decreases slightly from 1.18 to 1.16. Although the change in ASI would decrease the solubility of apatite, this may be counteracted by the additional melt generation during biotite breakdown and apatite growth is not expected.

In the absence of biotite, melting continues through the breakdown of quartz, plagioclase and K-feldspar, which results in a progressively drier melt. Monazite and zircon are predicted to be completely consumed by 820°C and 850°C, respectively. The increase in pressure near the metamorphic peak results in minor cordierite consumption to produce garnet. At the metamorphic peak, the metapelite has generated ~44 mol% melt.

Isobaric cooling at 6.5 kbar from 860°C to 750°C results in: (1) melt crystallization; (2) new zircon and monazite growth commencing at 855°C and 825°C, respectively; (3) a decrease in melt ASI, which would decrease the solubility of apatite and contribute to apatite crystallization; (4) the retrogression of cordierite and garnet to biotite; (5) the consumption of K-feldspar and the growth of plagioclase; and (6) a decrease in a_{TiO2}. The concurrent breakdown of garnet and growth of zircon, monazite and plagioclase may result in elevated HREE and Y concentrations and more pronounced negative Eu anomalies in newly crystallized accessory minerals. New zircon growth occurs when the a_{TiO2} value of the system ranges from 0.6 to 0.7. Applying the Ti-in-zircon thermometer assuming an a_{TiO2} value of 1.0 would underestimate the true temperature by ~50°C (Fig. 1b). Protracted retrograde monazite and zircon growth is expected during melt crystallization along the isobaric cooling segment of the counterclockwise *P–T* path (e.g., Korhonen et al. 2013b)

Greywacke

Phase relations. The pseudosection for the greywacke is shown in Figure 9. When compared with the metapelite, the greywacke composition is less fertile (e.g., Clemens and

Vielzeuf 1987; Thompson 1996; Vielzeuf and Schmidt 2001; Johnson et al. 2008; Yakymchuk and Brown 2014a), contains different mineral assemblages, and yields different reaction sequences. For the greywacke, quartz, ilmenite, plagioclase and garnet are stable across the entire diagram. Cordierite becomes stable at pressures of 5–7 kbar with increasing temperature. Orthopyroxene is stable at $P < 6$ kbar and $T > 800$°C. Rutile is stable at $P > 9$–11 kbar. Muscovite is stable at $P > 7$–12 kbar with increasing temperature. Similar to the metapelite, partial melting of the greywacke begins at the wet solidus at temperatures of ~670–700°C. A narrow low-variance field representing the breakdown of muscovite to produce K-feldspar is restricted to $P > 10.8$ kbar; this contrasts with a similar field in the metapelite pseudosection that extends from < 4 to > 12 kbar (Fig. 7). For the greywacke composition, biotite breakdown generates garnet at high pressure, cordierite at low pressure, and orthopyroxene at low pressure and high temperature.

Reaction sequence for the clockwise P–T path. The mode-box and titania activity for the clockwise assemblage sequence are shown in Figure 10a. The predicted amount of monazite and zircon remaining along with the ASI of melt are shown in Figure 10b. Along the clockwise *P*–*T* path, partial melting begins at ~675°C at the wet solidus and muscovite is not stable. Therefore, further melting proceeds through the breakdown of biotite and sillimanite to produce garnet. Similar to the metapelite, growing garnet has the potential to capture inherited or prograde monazite and zircon allowing their preservation to higher temperatures. K-feldspar becomes stable at 800°C and 8.2 kbar and biotite is completely consumed by 850°C. Up to this point, the greywacke has produced 14 mol% melt, which is less than the 34 mol% melt generated by the pelite for the same *P*–*T* path. Up to 850°C, melt is produced gradually for the greywacke composition whereas melting of the metapelite occurs as a pulse in the narrow muscovite–K-feldspar field followed by more gradual melting due to biotite breakdown.

Beyond the loss of biotite from the stable assemblage, melting continues through the breakdown of K-feldspar, plagioclase and quartz and an additional 4 mol% melt is produced by 900°C. Although monazite dissolution is modelled to continue from 850 to 900°C, some prograde monazite crystallization may be possible in this temperature range for three reasons. First, the melt is saturated with respect to LREE due to progressive monazite dissolution. Second, after the exhaustion of biotite the melt becomes progressively drier, which decreases the solubility of monazite. Third, melt ASI increases, which increases the dissolution of apatite and may liberate enough LREE to support new monazite growth. However, unless this monazite is sequestered away in a growing peritectic mineral (such as garnet) it is expected to be consumed during further heating and partial melting.

All of the monazite and ~65% of the zircon are consumed by 900°C. Isothermal decompression from 9 kbar to 7 kbar produces an additional 4 mol% melt and results in minor (<1 mol%) garnet consumption. Melt ASI increases from 1.18 to 1.23 during decompression, which enhances the solubility of apatite. However, the melt is undersaturated with respect to LREE and new monazite growth is not expected during decompression. Approximately 10% of the initial amount of zircon present at the solidus is consumed during decompression and titania activity decreases from 0.95 to 0.85.

Cooling and decompression from peak T to 750°C results in: (1) melt crystallization, (2) the consumption of garnet and sillimanite to produce cordierite commencing at 890°C and biotite starting at 840°C, (3) a decrease in a_{TiO2} from 0.85 to 0.65, (4) a decrease in melt ASI from 1.23 to 1.16, (5) the growth of new zircon (likely as overgrowths on existing zircon), and (6) the crystallization of monazite starting at ~885°C. Zircon and monazite growth occurs during garnet breakdown and these accessory minerals are expected to have elevated Y and HREE concentrations. The application of Ti-in-zircon thermometry should use an a_{TiO2} value ranging from 0.85 to 0.65. Assuming a a_{TiO2} value of 1.0 would underestimate temperatures by up to 50°C (Fig. 1b).

Reaction sequence for the counterclockwise P–T path. The mode-box and titania activity for the counterclockwise assemblage sequence are shown in Figure 10c. The amount of monazite and zircon remaining as well as melt ASI are shown in Figure 10d. Similar to the clockwise *P–T* path for the greywacke, the prograde segment of the counterclockwise *P–T* path generates melt gradually in contrast to the more pulsed melting in the metapelite. Melting commences at the wet solidus and proceeds via the breakdown of biotite to produce cordierite and garnet followed by K-feldspar at 760°C. Orthopyroxene enters the phase assemblage at 825°C and biotite is completely consumed by 830°C. The value of a_{TiO2} decreases from ~0.80 to 0.60 up to the orthopyroxene-in field boundary and then increases for the remainder of the prograde path. The increase in pressure near peak *T* results in the breakdown of orthopyroxene to produce garnet (e.g., White et al. 2008). By the end of the heating segment, ~50% of the zircon and ~70% of the monazite that was present at the solidus has been consumed. Melt ASI varies between 1.16 and 1.11 during the prograde path. As with the clockwise *P–T* path, melting above the biotite-stability field (in this case from 830–860°C) has the potential to generate some prograde monazite if LREE-rich apatite is consumed. A total of 18 mol% melt is predicted to be generated during heating, which is significantly less than the 44 mol% produced along the same *P–T* path for the metapelite.

Consistent with the metapelite for the same *P–T* path, isobaric cooling results in melt crystallization and monazite and zircon growth. The mode of garnet decreases by 7 mol% and K-feldspar breaks down to sillimanite in the presence of melt at 815°C. Zircon and monazite crystallization is predicted to have elevated Y and HREE due to the breakdown of garnet. Zircon growth occurs when the a_{TiO2} value of the system is ~0.7.

Average Mid Ocean Ridge Basalt

Phase relations. The *P–T* pseudosection for an average MORB composition is shown in Figure 11. The wet solidus has a negative slope from 4 to 11.5 kbar and a positive slope at *T* >11.5 kbar. The temperature of the wet solidus ranges from 620 to 700°C over the modelled *P–T* range. Garnet is stable from 10–14 kbar with decreasing temperature. Orthopyroxene enters the assemblage at temperatures of 800°C to 900°C with increasing *P* and is not stable above 10 kbar at high *T*. Garnet and orthopyroxene are only stable together at pressures of 9.5–10 kbar and at *T* > 900°C. Rutile is stable at $T > 790$°C at $P > 7$ kbar.

Reaction sequence for the clockwise P–T path. The mode-box and titania activity for the reaction sequence as well as the amount of zircon remaining and melt ASI are shown in Figure 12. Melting starts at the wet solidus at 630°C and 9.7 kbar and generates ~ 2 mol% melt and ~ 2 mol% clinopyroxene at the expense of epidote and biotite. A minor amount (~2 mol%) of zircon is expected to be consumed in order to saturate the melt in Zr. Epidote can be an important source of Zr (e.g., Kohn et al. 2015) and the breakdown of Zr-rich epidote may result in Zr saturation and minor zircon crystallization at this stage. After the exhaustion of biotite at ~650°C, melting continues via the breakdown of hornblende, titanite and quartz to produce an additional 4 mol% melt as well as peritectic clinopyroxene by 800°C and 11.4 kbar. During this portion of the prograde path, a_{TiO2} increases from 0.6 at the wet solidus up to 0.9 at 800°C. The amount of zircon remaining is ~80 mol% of the amount present at the solidus. Melt ASI increases slightly from 0.99 to 1.00.

Garnet becomes stable at ~800°C and melting proceeds through the breakdown of hornblende and titanite. Garnet growth may include zircon grains that would be isolated from the reacting volume of the rock and zircon could be preserved to higher *T*. Rutile becomes stable at 818°C and titanite is completely consumed by 821°C. The peak pressure of 12 kbar is reached at 850°C and at this point the system contains ~13 mol% melt, 10 mol% garnet and 65% of the zircon has been consumed. Although zircon is expected to be consumed during partial melting, the breakdown of Zr-rich amphibole (e.g., Sláma et al. 2007) may yield enough Zr to oversaturate the melt and grow new zircon; this zircon may be relatively depleted in HREE in response to the presence of garnet in the rock.

The isobaric heating segment of the *P*–*T* path at peak *P* produces garnet at the expense of hornblende and quartz. Quartz is exhausted at 905°C. This has implications for applying the Ti-in-zircon thermometer, which uses a_{SiO2} as a variable. Zircon is completely consumed by 880°C and the melt produced at higher *T* is expected to be undersaturated in Zr. A consequence of this is that prograde zircon growth at $T > 880$°C is unlikely because any excess Zr due to the breakdown of other minerals (e.g., amphibole) will be incorporated into the Zr-undersaturated melt. At the metamorphic peak of 950°C, the system contains ~28 mol% melt, ~20 mol% garnet and ~14% hornblende.

Isothermal decompression from 12 to 10 kbar results in significant garnet consumption (from 20 to 9 mol%), hornblende growth (from 14 to 24 mol%) and minor melt consumption (from 28 to 27 mol%). Zirconium liberated from garnet breakdown is expected to be partitioned between the Zr-undersaturated melt and hornblende. Consequently, zircon crystallization is unlikely. Orthopyroxene enters the assemblage at 10.1 kbar and grows at the expense of garnet, which is exhausted by 9.7 kbar. If garnet is completely consumed, any liberated zircon may become available to the reacting volume and will likely be consumed into the Zr-undersaturated melt. Rutile is completely consumed by 9.1 kbar and a_{TiO2} decreases with further decompression. At the end of the isothermal decompression segment of the *P–T* path the amount of orthopyroxene reaches 5 mol%. No new zircon growth is expected during the isothermal decompression segment because: (1) there is a <1 mol% melt change during isothermal decompression and the melt is already significantly undersaturated in Zr, (2) the *M* value of the melt (cation ratio of [Na + K + 2Ca]/ [Al x Si]) increases from 1.6 to 1.7, which results in an increases the Zr required to saturate the melt (Harrison and Watson 1983; Boehnke et al. 2013), (3) the mode of hornblende increases from 14 to 23 mol%, likely accommodating significant amounts of Zr at high temperature (e.g., Kohn et al. 2015).

Cooling and decompression from 950°C at 8 kbar to 800°C at 6 kbar results in the consumption of 17 mol% melt and the complete breakdown of orthopyroxene by ~830°C. Zirconium saturation of the melt is reached at ~870°C and zircon begins to crystallize. At ~850°C, approximately 20% of the amount of zircon originally present at the solidus has grown back and this zircon expected to be enriched in HREE because there is no garnet present in the system. Zircon growth at this stage occurs in a system with an a_{TiO2} value of 0.9 and in the absence of quartz, which is important for the application of Ti-in-zircon thermometry.

Summary of reaction sequence modelling

Linking the trace element concentrations of accessory minerals to the key major minerals (e.g., garnet and plagioclase) requires an understanding of the reaction sequences for a particular bulk composition. Key minerals like garnet and plagioclase can grow or be consumed multiple times along a *P–T* path during heating and cooling or burial and exhumation (Figs 3–10). For example, garnet is predicted to grow in the subsolidus greywacke composition during heating and burial and garnet breakdown occurs during cooling and exhumation for the hairpin *P–T* path (Fig. 6b). By contrast, garnet growth and consumption occurs multiple times along the heating and increasing pressure segment of the *P–T* paths for the subsolidus metapelite composition (Fig. 4). Therefore, high-Y and high-HREE zones in monazite that can be linked to garnet breakdown may reflect the burial and/or exhumation portions of a *P–T* path.

Titania activity also varies along the modelled *P–T* paths and this needs to be taken into account when applying Ti-in-zircon or Ti-in-quartz thermometers. In general, new zircon growth in subsolidus rocks is expected to be limited because major minerals such as hornblende and garnet can accommodate more Zr with increasing temperature. One exception to this may be minor zircon growth through the breakdown of Zr-rich epidote. For the suprasolidus *P–T* paths for the metapelite and greywacke, new zircon growth is expected during cooling and melt crystallization; this growth is predicted to occur when bulk rock a_{TiO2} is less than one for all of the modelled *P–T* paths. If the Ti-in-zircon thermometer is applied with an a_{TiO2} value of one, then the result will be an underestimation in peak metamorphic temperatures by up to ~40°C. For the MORB composition, new zircon growth occurs at $a_{\mathrm{TiO2}} < 1.0$ as cooling and melt crystallization occurs outside the stability field of rutile (Fig. 12).

In suprasolidus metamorphic rocks, zircon and monazite are expected to be consumed along the prograde path and new growth is generally predicted to occur along the cooling path.

Zircon and monazite dissolution is non-linear and the rate increases with increasing temperature. For the clockwise *P–T* path for the metapelite and greywacke, an increase in the melt ASI leads to more apatite dissolution. Because the melt is saturated in LREE with respect to monazite up to 820°C, apatite breakdown may liberate enough LREE to promote new monazite growth. However, after the exhaustion of monazite, the melt is expected to be undersaturated in LREE and prograde monazite growth at the expense of LREE-rich apatite is unlikely. For the counterclockwise *P–T* path for the metapelite and greywacke, melt ASI increases and decreases during the *P–T* evolution and monazite growth from apatite breakdown will be more complex to interpret.

The metapelite is expected to lose most of the inherited or subsolidus prograde monazite and zircon during heating above the solidus (unless these mineral are sequestered away from the reaction volume) whereas a larger proportion of these minerals remains in the greywacke composition except for the clockwise *P–T* path where monazite is completely consumed for the greywacke. The difference reflects the fertility of the two rocks; pelites generate more melt than the greywacke and require more Zr and LREE to saturate this melt. Therefore, less fertile compositions, such as greywackes, are more likely to preserve subsolidus zircon and monazite.

COMPLICATING FACTORS

Changes in effective bulk composition

Phase equilibria modelling requires an assessment of the effective bulk composition of a system that is used to model the *P–T* phase relations for a rock (e.g., Stüwe 1997). The effective bulk composition approximates the composition ‘available’ to the rock in which equilibrated mineral assemblages and reaction sequence develop. In natural systems, the effective bulk composition may change along a *P–T* path (e.g., Guevara and Caddick 2016), which has subsequent implications for modelling reaction sequences in both subsolidus and suprasolidus metamorphic rocks. There are two main mechanisms that can change the effective bulk composition of a metamorphic system: fractionation of elements into growing porphyroblasts and melt loss.

Growing porphyroblasts can fractionate certain elements into their cores that become unavailable to the reacting system in the remainder of the rock. For example, chemical zoning in garnet is commonly preserved in metamorphic rocks because cation diffusion in garnet is relatively slow (e.g., Chakraborty and Ganguly 1992). The preferential partitioning of elements into garnet cores reduces their effective composition in the reactive volume of the rock (e.g., Lanari and Engi, 2017). Some of the consequences for using phase diagrams to infer metamorphic conditions considering garnet fractionation include reduced stability fields for garnet (Gaides et al. 2008) and other minerals (Zuluaga et al. 2005; Moynihan and Pattison 2013) as well as changes in mineral compositional isopleths for garnet (Evans 2004; Gaides et al. 2006) and plagioclase (Moynihan and Pattison 2013). While crystal fractionation needs to be assessed on a case-by-case basis, it is generally most important to consider for greenschist- and amphibolite-facies metamorphic assemblages where mineral chemistries are particularity useful for determining *P–T* conditions. At higher grades, the use of mineral composition isopleths is generally less effective due to retrograde exchange reactions (e.g., Spear and Florence 1992; Kohn and Spear 2000; Pattison et al. 2003). For zircon, the fractionation of Zr into growing garnet (e.g., Kohn et al. 2015) may reduce the Zr budget available for zircon growth.

In high-grade metamorphic rocks that underwent anatexis the preservation of peritectic minerals and lack of extensive retrogression supports melt drainage during prograde metamorphism (Fyfe 1973; Powell 1983; White and Powell 2002; Guernina and Sawyer 2003; Reno et al. 2012). Melt loss produces progressively more refractory bulk compositions, which results in elevated solidus temperatures in the residual rocks. In migmatites that have undergone melt loss, suprasolidus zircon and monazite growth is generally expected to occur during cooling from peak *T* to the elevated solidus (e.g., Kelsey et al. 2008; Spear and Pyle 2010; Yakymchuk and Brown 2014b). Therefore, rocks that have experienced identical *P–T* histories but variable amounts of melt loss and have different solidus temperatures should record a range of ages (e.g., Korhonen et al. 2013b).

Bulk composition and the suprasolidus behaviour of zircon and monazite

For the modelled suprasolidus reaction sequences, the preservation of subsolidus (e.g., prograde or inherited) zircon and monazite is mainly related to the fertility of the rocks. The metapelite generates more melt along the same *P–T* path than the greywacke. Consequently, zircon and monazite are completely consumed for the metapelite composition along both *P–T* paths (Figs 8a, b) whereas some zircon and/or monazite can survive in the greywacke. An additional factor is the bulk rock content of Zr for zircon and LREE and phosphorus for monazite (e.g., Kelsey et al. 2008; Yakymchuk and Brown 2014b). Both of these factors are explored together in Figure 13.

The temperature–composition diagrams in Figure 13 illustrate the variation in melt mode and the stability of zircon and monazite for compositions ranging linearly from the metapelite (left side) to that of the greywacke (right side). The diagrams are isobaric and were calculated at 7 kbar because this pressure intersects the main melt producing reactions for both bulk compositions. The common reaction to both compositions is the breakdown of biotite to produce cordierite at ~840–845°C (Fig. 13a). The amount of melt in the metapelite composition is roughly twice the amount in the greywacke composition over the range of modelled temperatures (Fig. 13b). For a bulk composition of 150 ppm Zr, zircon is completely consumed in the metapelite composition by 925°C whereas only 30% of the zircon has been consumed in the greywacke composition at the same temperature (Fig. 13c). For a bulk composition of 150 ppm LREE, monazite is completely consumed by 830°C for the metapelite and 880°C for the greywacke (Fig. 13d). The slopes of the dissolution contours are steeper for zircon than for monazite in Figures 13c and 13d. This indicates that zircon dissolution is more sensitive to bulk composition (metapelite vs. greywacke) than monazite.

The sensitivity of zircon and monazite dissolution to bulk composition of Zr and LREE is explored in Figures 13e and 13f. The contours represent the complete dissolution of zircon and monazite for various bulk rock Zr and LREE contents. For low-Zr pelites with concentrations of 50 ppm, zircon is completely consumed by 860°C, which is 65°C lower than for a closer-to-average Zr concentration of 150 ppm. Greywackes with low concentrations of Zr (e.g., 50 ppm) can still preserve zircon up to UHT conditions due to their lower fertility. Monazite dissolution contours in Figure 13f have shallower slopes than those for zircon (Fig. 13e), which again suggests that monazite dissolution is less sensitive to bulk composition. A metapelite with low concentrations of LREE (e.g., 50 ppm) is predicted to lose monazite by 780°C and monazite is expected to be completely consumed in the greywacke composition by 820°C. Preserving subsolidus monazite to UHT conditions requires very LREE-rich compositions of >400 ppm for the metapelite and >180 ppm for the greywacke. Therefore, a strategy for finding subsolidus prograde zircon and monazite in migmatites is to choose samples with the highest concentrations of Zr and LREE.

The breakdown of LREE-rich apatite is a potential mechanism to promote prograde suprasolidus monazite growth (e.g., Johnson et al. 2015). This is most likely to occur when the anatectic melt is saturated with respect to monazite in LREE. After the exhaustion of monazite, the melt is expected to be undersaturated and LREE liberated from the breakdown of apatite is not predicted to generate new prograde monazite growth. In principle, the higher the bulk rock LREE the longer monazite will persist during a suprasolidus heating path and the longer the melt will remain saturated with respect to LREE (Fig. 13f). A further consideration is that bulk compositions with low phosphorus concentrations may lose apatite during the prograde path and would result in melt that is undersaturated in P. This may promote further monazite dissolution instead of monazite growth. Therefore, LREE and P-rich bulk compositions should be targeted for accessory mineral geochronology to constrain the timing of suprasolidus prograde monazite growth.

Effects of open system behaviour on accessory minerals

Dissolution/re-precipitation of accessory minerals in metamorphic rocks due to the infiltration of an externally derived fluid has been documented in experiments and studies of natural samples (e.g., Tomaschek et al. 2003; Crowley et al. 2008; Harlov and Hetherington 2010; Blereau et al. 2016). The careful integration of petrography with the chemistries of these minerals can be used to provide information on the timing of fluid infiltration (e.g., Williams et al. 2011) and on fluid chemistry (e.g., Harlov et al. 2011; Taylor et al. 2014; Shazia et al. 2015). However, the timing of fluid ingress relative to the metamorphic history and the chemistry of these fluids are highly variable and should to be assessed on a case-by-case basis.

For migmatites that have lost melt, the extraction of melt saturated in Zr or LREE will also change the effective composition of the residuum (e.g., Rapp et al. 1987), which has subsequent consequences for zircon and monazite dissolution. For example, consider the muscovite to K-feldspar melting reaction for the metapelite along the clockwise *P–T* path at ~730°C and 7.5 kbar and consider bulk rock values of 150 ppm for LREE and Zr. This reaction involves a large positive volume change (e.g., Powell et al. 2005), which may be accommodated by melt extraction from the rock. When muscovite is exhausted the rock contains ~9 mol% melt. The saturation concentrations of LREE and Zr in the melt at this point are 195 ppm and 137 ppm, respectively. Assuming 8 vol% melt (approximately equivalent to 8 mol%) is extracted (leaving 1 vol% in the rock along grain boundaries), mass balance can be used to determine the amount of Zr and LREE left in the system. For this example, the effective concentration of LREE in the rock decreases to 146 ppm and the effective concentration of Zr increases to 151 ppm. Although the changes to the bulk composition are minor in this example, monazite is predicted to be completely consumed at lower *T* and zircon may persist to higher *T* than for closed system (Fig. 13). For rocks with very low concentrations of Zr and LREE, melt extraction can have a more significant impact on the effective bulk concentrations of these elements and the stability of zircon and monazite (e.g., Yakymchuk and Brown 2014b).

Inclusion/host relationships

An important consideration for accessory mineral reactivity is their inclusion in the major rock-forming minerals (Watson et al. 1989; Bea et al. 2006). Watson et al. (1989) showed that for a Himalayan migmatite sample roughly 78% of the zircon mass is located along grain boundaries and the remaining 28% is included in major minerals (predominately biotite and garnet), though how representative this is of typical migmatitic gneiss is unknown. Consequently, the breakdown of major minerals may liberate accessory minerals into the reacting volume of the rock that would otherwise be sequestered away.

Inclusions of zircon and monazite that are isolated from the reaction volume may also reduce the effective bulk rock concentration of Zr and LREE (Yakymchuk and Brown 2014b). For example, consider a bulk rock composition of LREE with half of the monazite sequestered away from the reaction volume as inclusions. For a metapelite with a bulk rock LREE composition of 300 ppm and considering that half of this is unavailable, the effective concentration of LREE is 150 ppm. The complete dissolution of monazite is modelled to occur at 830°C in contrast to 870°C for the scenario where all monazite is available for reaction (Fig. 13f). Therefore, applying the models in Figure 13 to natural examples requires an estimate of the amount of zircon or monazite sequestered away from the reaction volume as inclusions as well as an estimate of the amount of Zr and LREE locked away in the major minerals.

The heterogeneous distribution of melt and minerals in high-grade metamorphic rocks also has implications for the dissolution and preservation of accessory minerals. Even for an initially homogenous protolith, *in situ* melt may be spatially associated with peritectic minerals in isolated patches; this produces a heterogeneous melt framework (e.g., White et al. 2004). Zircon and monazite proximal to the zones of incipient melting and in chemical communication with this melt are more likely to contribute to Zr and LREE saturation of the melt whereas more distal grains may not. Consequently, detrital, inherited or prograde (subsolidus or early suprasolidus) zircon and monazite are more likely to be preserved in domains away from incipient melting whereas post-peak and retrograde zircon and monazite may be spatially associated with *in situ* leucosome.

CONCLUDING REMARKS

One important facet of petrochronology is to link the ages of accessory mineral chronometers to the *P–T* information obtained from major rock-forming minerals in metamorphic rocks. The growth and consumption of major minerals is important because these minerals: (1) may contain the necessary essential structural constituents to promote accessory mineral growth directly from their breakdown, (2) are repositories of the trace elements used to link accessory mineral chronometers to *P–T* conditions (e.g., Sr and Eu related to stability of plagioclase as well as Y and HREE reflecting the growth/consumption of garnet), (3) are important hosts for accessory mineral inclusions, and (4) play a role in controlling the component activities (e.g., a_{TiO2}) along a *P–T* evolution. The main controls on accessory mineral behaviour differ between subsolidus and suprasolidus metamorphic conditions.

For subsolidus metamorphism, zircon is generally unreactive and monazite can grow during the prograde and retrograde segments. Linking ages from these accessory mineral to a metamorphic history requires an understanding of the major mineral reaction sequence as well as the behaviour of accessory minerals like xenotime, apatite and allanite. Major minerals such as garnet or plagioclase may experience growth and breakdown stages at any point along a *P–T* path: linking their behaviour to the trace element chemistries of accessory minerals requires an assessment of the reaction sequence for a particular rock along a well-constrained *P–T* path.

For suprasolidus metamorphism, phase equilibria modelling predicts that both zircon and monazite will be consumed during prograde metamorphism and grow during cooling and melt crystallization. However, this contrasts with some studies that have convincingly showed evidence for suprasolidus prograde zircon and monazite growth. For monazite, apatite dissolution may have contributed to minor prograde monazite growth if the anatectic melt is saturated in LREE. For zircon, solid-state breakdown of major minerals that contain appreciable quantities of Zr may facilitate prograde zircon growth. Ostwald ripening may also play a role in the prograde growth of both zircon and monazite, but this mechanism is still incompletely understood.

Acknowledgements

We thank Mark Caddick and Dave Waters for thorough and perceptive reviews and Pierre Lanari for his patient editorial work. Nonetheless, the authors are responsible for any misinterpretations or omissions that persist. CY was partially funded by a National Sciences and Engineering Research Council of Canada Discovery Grant.

References

Ague JJ (1991) Evidence for major mass transfer and volume strain during regional metamorphism of pelites. Geology 19:855–858

Ashley KT, Law RD (2015) Modeling prograde TiO2 activity and its significance for Ti-in-quartz thermobarometry of pelitic metamorphic rocks. Contr Mineral and Petrol 169:1–7

Ayers JC, Miller C, Gorisch B, Milleman J (1999) Textural development of monazite during high-grade metamorphism: Hydrothermal growth kinetics, with implications for U, Th-Pb geochronology. Am Mineral 84:1766–1780

Baxter EF, Scherer EE (2013) Garnet geochronology: timekeeper of tectonometamorphic processes. Elements 9:433–438

Baxter EF (2017) Title of Chapter. Rev Mineral Geochem XX:xxx–xxx.

Bea F, Pereira MD, Stroh A (1994) Mineral/leucosome trace-element partitioning in a peraluminous migmatite (a laser ablation-ICP-MS study). Chem Geol 117:291–312

Bea F, Montero P (1999) Behavior of accessory phases and redistribution of Zr, REE, Y, Th, and U during metamorphism and partial melting of metapelites in the lower crust: an example from the Kinzigite Formation of Ivrea-Verbano, NW Italy. Geochim Cosmochim Acta 63:1133-1153

Bea F, Montero P, Ortega M (2006) A LA–ICP–MS evaluation of Zr reservoirs in common crustal rocks: implications for Zr and Hf geochemistry, and zircon-forming processes. Can Mineral 44:693–714

Berman RG (1988) Internally-consistent thermodynamic data for minerals in the system Na2O-K2O-CaO-MgO-FeO-Fe2O3-Al2O3-SiO2-TiO2-H2O-CO2. J Petrol 29:445–522

Bingen B, Austrheim H, Whitehouse M (2001) Ilmenite as a source for zirconium during high-grade metamorphism? Textural evidence from the Caledonides of Western Norway and implications for zircon geochronology. J Petrol 42:355–375

Blereau E, Clark C, Taylor RJM, Johnson TJ, Fitzsimons I, Santosh M (2016) Constraints on the timing and conditions of high-grade metamorphism, charnockite formation and fluid-rock interaction in the Trivandrum Block, southern India. J Metamorph Geol 34:527–549.

Boehnke P, Watson EB, Trail D, Harrison TM, Schmitt AK (2013) Zircon saturation re-revisited. Chem Geol 351:324–334

Brown M (1998) Unpairing metamorphic belts: P–T paths and a tectonic model for the Ryoke Belt, southwest Japan. J Metamorph Geol 16:3–22

Brown M (2014) The contribution of metamorphic petrology to understanding lithosphere evolution and geodynamics. Geosci Front 5:553–569

Brown M, Kothonen FJ (2009) Some remarks on melting and extreme metamorphism of crustal rocks. *In*: Physics and Chemistry of the Earth's Interior. Gupta AK and Dasgupta S (eds) Springer, p 67–87

Caddick MJ, Kohn MJ (2013) Garnet: Witness to the evolution of destructive plate boundaries. Elements 9:427–432

Carlson WD (1999) The case against Ostwald ripening of porphyroblasts. Can Mineral 37:403–414

Carlson WD (2000) The case against Ostwald ripening of porphyroblasts: reply. Can Mineral 38:1029–1031

Catlos EJ, Harrison TM, Kohn MJ, Grove M, Ryerson FJ, Manning CE, Upreti BN (2001) Geochronologic and thermobarometric constraints on the evolution of the Main Central Thrust, central Nepal Himalaya. J Geophys Res B: Solid Earth 106:16177–16204

Chakraborty S, Ganguly J (1992) Cation diffusion in aluminosilicate garnets: experimental determination in spessartine-almandine diffusion couples, evaluation of effective binary diffusion coefficients, and applications. Contr Mineral and Petrol 111:74–86

Chambers JA, Kohn MJ (2012) Titanium in muscovite, biotite, and hornblende: Modeling, thermometry, and rutile activities of metapelites and amphibolites. Am Mineral 97:543–555

Chen Y-X, Zheng Y-F, Hu Z (2013) Synexhumation anatexis of ultrahigh-pressure metamorphic rocks: petrological evidence from granitic gneiss in the Sulu orogen. Lithos 156:69–96

Clark C, Fitzsimons ICW, Healy D, Harley SL (2011) How does the continental crust get really hot? Elements 7:235–240

Clark C, Kirkland CL, Spaggiari CV, Oorschot C, Wingate MTD, Taylor RJ (2014) Proterozoic granulite formation driven by mafic magmatism: An example from the Fraser Range Metamorphics, Western Australia. Precambrian Res 240:1–21

Clark DJ, Hensen BJ, Kinny PD (2000) Geochronological constraints for a two-stage history of the Albany–Fraser Orogen, Western Australia. Precambrian Res 102:155-183

Clarke GL, Guiraud M, Powell R, Burg JP (1987) Metamorphism in the Olary Block, South Australia: compression with cooling in a Proterozoic fold belt. J Metamorph Geol 5:291–306

Clemens JD, Vielzeuf D (1987) Constraints on melting and magma production in the crust. Earth Planet Sci Lett 86:287–306

Collins WJ, Vernon RH (1991) Orogeny associated with anticlockwise PTt paths: Evidence from low-P, high-T metamorphic terranes in the Arunta inlier, central Australia. Geology 19:835–838

Connolly JAD, Petrini K (2002) An automated strategy for calculation of phase diagram sections and retrieval of rock properties as a function of physical conditions. J Metamorph Geol 20:697–708

Copeland RA, Frey FA, Wones DR (1971) Origin of clay minerals in a Mid-Atlantic Ridge sediment. Earth Planet Sci Lett 10:186–192

Corrie SL, Kohn MJ (2008) Trace-element distributions in silicates during prograde metamorphic reactions: Implications for monazite formation. J Metamorph Geol 26:451–464

Crowley JL, Brown RL, Gervais F, Gibson HD (2008) Assessing inheritance of zircon and monazite in granitic rocks from the Monashee Complex, Canadian Cordillera. J Petrol 49:1915–1929

Crowley JL, Waters DJ, Searle MP, Bowring SA (2009) Pleistocene melting and rapid exhumation of the Nanga Parbat massif, Pakistan: Age and P–T conditions of accessory mineral growth in migmatite and leucogranite. Earth Planet Sci Lett 288:408–420

Dawson GC, Krapež B, Fletcher IR, McNaughton NJ, Rasmussen B (2003) 1.2 Ga thermal metamorphism in the Albany–Fraser Orogen of Western Australia: consequence of collision or regional heating by dyke swarms? J Geol Soc London 160:29–37

de Capitani C, Brown TH (1987) The computation of chemical equilibrium in complex systems containing non-ideal solutions. Geochim Cosmochim Acta 51:2639–2652

de Capitani C, Petrakakis K (2010) The computation of equilibrium assemblage diagrams with Theriak/Domino software. Am Mineral 95:1006–1016

Degeling H, Eggins S, Ellis DJ (2001) Zr budgets for metamorphic reactions, and the formation of zircon from garnet breakdown. Mineral Mag 65:749–758

Diener JFA, Powell R (2010) Influence of ferric iron on the stability of mineral assemblages. J Metamorph Geol 28:599–613

Dragovic B, Baxter EF, Caddick MJ (2015) Pulsed dehydration and garnet growth during subduction revealed by zoned garnet geochronology and thermodynamic modeling, Sifnos, Greece. Earth Planet Sci Lett 413:111-122

Dragovic B, Samanta LM, Baxter EF, Selverstone J (2012) Using garnet to constrain the duration and rate of water-releasing metamorphic reactions during subduction: an example from Sifnos, Greece. Chem Geol 314:9–22

Dragovic B, Guevara VE, Caddick MJ, Baxter EF, Kylander-Clark ARC (2016) A pulse of cryptic granulite-facies metamorphism in the Archean Wyoming Craton revealed by Sm–Nd garnet and U–Pb monazite geochronology. Precambrian Res 283:24–49

Duc-Tin Q, Keppler H (2015) Monazite and xenotime solubility in granitic melts and the origin of the lanthanide tetrad effect. Contr Mineral and Petrol 169:1–26

Enami M, Liou JG, Mattinson CG (2004) Epidote minerals in high P/T metamorphic terranes: Subduction zone and high-to ultrahigh-pressure metamorphism. Rev Mineral Geochem 56:347–398

Engi (2017) Title of Chapter. Rev Mineral Geochem XX:xxx–xxx.

England PC, Thompson AB (1984) Pressure—Temperature—Time Paths of Regional Metamorphism I. Heat Transfer during the Evolution of Regions of Thickened Continental Crust. J Petrol 25:894–928

Evans TP (2004) A method for calculating effective bulk composition modification due to crystal fractionation in garnet-bearing schist: implications for isopleth thermobarometry. J Metamorph Geol 22:547–557

Ewing TA, Rubatto D, Hermann J (2014) Hafnium isotopes and Zr/Hf of rutile and zircon from lower crustal metapelites (Ivrea–Verbano Zone, Italy): implications for chemical differentiation of the crust. Earth Planet Sci Lett 389:106-118

Ferry JM, Watson EB (2007) New thermodynamic models and revised calibrations for the Ti-in-zircon and Zr-in-rutile thermometers. Contr Mineral and Petrol 154:429–437

Finger F, Krenn E (2007) Three metamorphic monazite generations in a high-pressure rock from the Bohemian Massif and the potentially important role of apatite in stimulating polyphase monazite growth along a PT loop. Lithos 95:103–115

Finger F, Krenn E, Schulz B, Harlov D, Schiller D (2016) "Satellite monazites" in polymetamorphic basement rocks of the Alps: Their origin and petrological significance. Am Mineral 101:1094–1103

Fitzsimons IC, Kinny PD, Wetherley S, Hollingsworth DA (2005) Bulk chemical control on metamorphic monazite growth in pelitic schists and implications for U–Pb age data. J Metamorph Geol 23:261–277

Florence FP, Spear FS (1993) Influences of reaction history and chemical diffusion on PT calculations for staurolite schists from the Littleton Formation, northwestern New Hampshire. Am Mineral 78:345–359

Foster G, Kinny P, Vance D, Prince C, Harris N (2000) The significance of monazite U–Th–Pb age data in metamorphic assemblages; a combined study of monazite and garnet chronometry. Earth Planet Sci Lett 181:327–340

Foster G, Gibson H, Parrish RR, Horstwood MSA, Fraser J, Tindle A (2002) Textural, chemical and isotopic insights into the nature and behaviour of metamorphic monazite. Chem Geol 191:183–207

Foster G, Parrish RR, Horstwood MS, Chenery S, Pyle J, Gibson HD (2004) The generation of prograde P–T–t points and paths; a textural, compositional, and chronological study of metamorphic monazite. Earth Planet Sci Lett 228:125–142

Franz G, Andrehs G, Rhede D (1996) Crystal chemistry of monazite and xenotime from Saxothuringian-Moldanubian metapelites, NE Bavaria, Germany. European Journal of Mineralogy:1097-1118

Franz G, Morteani G, Rhede D (2015) Xenotime-(Y) formation from zircon dissolution–precipitation and HREE fractionation: an example from a metamorphosed phosphatic sandstone, Espinhaço fold belt (Brazil). Contr Mineral and Petrol 170:1–22

Fraser G, Ellis D, Eggins S (1997) Zirconium abundance in granulite-facies minerals, with implications for zircon geochronology in high-grade rocks. Geology 25:607–610

Frei D, Liebscher A, Franz G, Dulski P (2004) Trace element geochemistry of epidote minerals. Rev Mineral Geochem 56:553–605

Frost BR, Chamberlain KR, Schumacher JC (2001) Sphene (titanite): phase relations and role as a geochronometer. Chem Geol 172:131–148

Fyfe WS (1973) The granulite facies, partial melting and the Archaean crust. Philos Trans R Soc London, Ser A 273:457–461

Gaidies F, Abart R, De Capitani C, Schuster R, Connolly JAD, Reusser E (2006) Characterization of polymetamorphism in the Austroalpine basement east of the Tauern Window using garnet isopleth thermobarometry. J Metamorph Geol 24:451–475

Gaidies F, De Capitani C, Abart R (2008) THERIA_G: a software program to numerically model prograde garnet growth. Contr Mineral and Petrol 155:657–671

Gaidies F, Pattison DRM, De Capitani C (2011) Toward a quantitative model of metamorphic nucleation and growth. Contr Mineral and Petrol 162:975–993

Gasser D, Bruand E, Rubatto D, Stüwe K (2012) The behaviour of monazite from greenschist facies phyllites to anatectic gneisses: an example from the Chugach Metamorphic Complex, southern Alaska. Lithos 134:108–122

Gervasoni F, Klemme S, Rocha-Júnior ERV, Berndt J (2016) Zircon saturation in silicate melts: a new and improved model for aluminous and alkaline melts. Contr Mineral and Petrol 171:1–12

Ghent ED (1976) Plagioclase-garnet-Al_2SiO_5-quartz: a potential geobarometer-geothermometer. Am Mineral 6:710–714

Gibson HD, Carr SD, Brown RL, Hamilton MA (2004) Correlations between chemical and age domains in monazite, and metamorphic reactions involving major pelitic phases: an integration of ID-TIMS and SHRIMP geochronology with Y–Th–U X-ray mapping. Chem Geol 211:237–260

Grapes RH, Hoskin PWO (2004) Epidote group minerals in low–medium pressure metamorphic terranes. Rev Mineral Geochem 56:301–345

Green ECR, White RW, Diener JFA, Powell R, Palin RM (2016) Activity–composition relations for the calculation of partial melting equilibria in metabasic rocks. J Metamorph Geol, doi: 10.1111/jmg.12211

Gromet LP, Silver LT (1983) Rare earth element distributions among minerals in a granodiorite and their petrogenetic implications. Geochim Cosmochim Acta 47:925-939

Guernina S, Sawyer EW (2003) Large-scale melt-depletion in granulite terranes: An example from the Archean Ashuanipi Subprovince of Quebec. J Metamorph Geol 21:181–201

Guevara VE, Caddick MJ (2016) Shooting at a moving target: phase equilibria modelling of high-temperature metamorphism. J Metamorph Geol 34:209–235.

Hacker BR, Andersen TB, Johnston S, Kylander-Clark ARC, Peterman EM, Walsh EO, Young D (2010) High-temperature deformation during continental-margin subduction & exhumation: The ultrahigh-pressure Western Gneiss Region of Norway. Tectonophysics 480:149–171

Hacker BR, Kylander-Clark ARC, Holder R, Andersen TB, Peterman EM, Walsh EO, Munnikhuis JK (2015) Monazite response to ultrahigh-pressure subduction from U–Pb dating by laser ablation split stream. Chem Geol 409:28–41

Harlov DE, Hetherington CJ (2010) Letter. Partial high-grade alteration of monazite using alkali-bearing fluids: Experiment and nature. Am Mineral 95:1105–1108

Harlov DE, Wirth R, Förster H-J (2005) An experimental study of dissolution–reprecipitation in fluorapatite: fluid infiltration and the formation of monazite. Contr Mineral and Petrol 150:268–286

Harlov DE, Wirth R, Hetherington CJ (2011) Fluid-mediated partial alteration in monazite: the role of coupled dissolution–reprecipitation in element redistribution and mass transfer. Contr Mineral and Petrol 162:329–348

Harris NBW, Caddick M, Kosler J, Goswami S, Vance D, Tindle AG (2004) The pressure–temperature–time path of migmatites from the Sikkim Himalaya. J Metamorph Geol 22:249–264

Harrison TM, Watson EB (1983) Kinetics of zircon dissolution and zirconium diffusion in granitic melts of variable water content. Contr Mineral and Petrol 84:66–72

Harrison TM, Watson EB (1984) The behavior of apatite during crustal anatexis: equilibrium and kinetic considerations. Geochim Cosmochim Acta 48:1467–1477

Hay DC, Dempster TJ (2009) Zircon behaviour during low-temperature metamorphism. J Petrol 50: 571–589.

Hayden LA, Watson EB, Wark DA (2008) A thermobarometer for sphene (titanite). Contr Mineral and Petrol 155:529–540

Hensen BJ (1971) Theoretical phase relations involving cordierite and garnet in the system MgO-FeO-Al2O3-SiO2. Contr Mineral and Petrol 33:191-214

Hermann J, Rubatto D (2003) Relating zircon and monazite domains to garnet growth zones: age and duration of granulite facies metamorphism in the Val Malenco lower crust. J Metamorph Geol 21:833-852

Hermann J, Rubatto D, Korsakov A, Shatsky VS (2001) Multiple zircon growth during fast exhumation of diamondiferous, deeply subducted continental crust (Kokchetav Massif, Kazakhstan). Contr Mineral and Petrol 141:66–82

Hiess J, Nutman AP, Bennett VC, Holden P (2008) Ti-in-zircon thermometry applied to contrasting Archean metamorphic and igneous systems. Chem Geol 247:323–338

Hofmann AE, Baker MB, Eiler JM (2013) An experimental study of Ti and Zr partitioning among zircon, rutile, and granitic melt. Contr Mineral and Petrol 166:235–253

Holder RM, Hacker BR, Kylander-Clark ARC, Cottle JM (2015) Monazite trace-element and isotopic signatures of (ultra) high-pressure metamorphism: Examples from the Western Gneiss Region, Norway. Chem Geol 409:99–111

Holland TJB, Powell R (1998) An internally consistent thermodynamic data set for phases of petrological interest. J Metamorph Geol 16:309–343

Holland TJB, Powell R (2011) An improved and extended internally consistent thermodynamic dataset for phases of petrological interest, involving a new equation of state for solids. J Metamorph Geol 29:333–383

Hoskin PWO, Schaltegger U (2003) The composition of zircon and igneous and metamorphic petrogenesis. Rev Mineral Geochem 53:27–62

Huang WL, Wyllie PJ (1973) Melting relations of muscovite-granite to 35 kbar as a model for fusion of metamorphosed subducted oceanic sediments. Contr Mineral and Petrol 42:1-14

Jamieson RA, Beaumont C, Medvedev S, Nguyen MH (2004) Crustal channel flows: 2. Numerical models with implications for metamorphism in the Himalayan-Tibetan orogen. J Geophys Res B: Solid Earth 109:2156–2202

Janots E, Engi M, Berger A, Allaz J, Schwarz JO, Spandler C (2008) Prograde metamorphic sequence of REE minerals in pelitic rocks of the Central Alps: implications for allanite–monazite–xenotime phase relations from 250 to 610 C. J Metamorph Geol 26:509–526

Janots E, Engi M, Rubatto D, Berger A, Gregory C, Rahn M (2009) Metamorphic rates in collisional orogeny from in situ allanite and monazite dating. Geology 37:11-14

Johnson TE, White RW, Powell R (2008) Partial melting of metagreywacke: a calculated mineral equilibria study. J Metamorph Geol 26:837-853

Johnson TE, Clark C, Taylor RJM, Santosh M, Collins AS (2015) Prograde and retrograde growth of monazite in migmatites: An example from the Nagercoil Block, southern India. Geosci Front 6:373–387

Kapp P, Manning CE, Tropper P (2009) Phase-equilibrium constraints on titanite and rutile activities in mafic epidote amphibolites and geobarometry using titanite-rutile equilibria. J Metamorph Geol 27:509–521

Kawakami T, Yamaguchi I, Miyake A, Shibata T, Maki K, Yokoyama TD, Hirata T (2013) Behavior of zircon in the upper-amphibolite to granulite facies schist/migmatite transition, Ryoke metamorphic belt, SW Japan: constraints from the melt inclusions in zircon. Contr Mineral and Petrol 165:575–591

Kelsey DE, Powell R (2011) Progress in linking accessory mineral growth and breakdown to major mineral evolution in metamorphic rocks: a thermodynamic approach in the Na2O-CaO-K2O-FeO-MgO-Al2O3-SiO2-H2O-TiO2-ZrO2 system. J Metamorph Geol 29:151–166

Kelsey DE, Hand M (2015) On ultrahigh temperature crustal metamorphism: phase equilibria, trace element thermometry, bulk composition, heat sources, timescales and tectonic settings. Geosci Front 6:311–356

Kelsey DE, Clark C, Hand M (2008) Thermobarometric modelling of zircon and monazite growth in melt-bearing systems: examples using model metapelitic and metapsammitic granulites. J Metamorph Geol 26:199–212

Kingsbury JA, Miller CF, Wooden JL, Harrison TM (1993) Monazite paragenesis and U-Pb systematics in rocks of the eastern Mojave Desert, California, USA: implications for thermochronometry. Chem Geol 110:147–167

Kirkland CL, Spaggiari CV, Johnson TE, Smithies RH, Danišík M, Evans N, Wingate MTD, Clark C, Spencer C, Mikucki E, McDonald BJ (2016) Grain size matters: Implications for element and isotopic mobility in titanite. Precambrian Res 278:283–302

Kohn MJ (2008) PTt data from central Nepal support critical taper and repudiate large-scale channel flow of the Greater Himalayan Sequence. Geol Soc Am Bull 120:259–273

Kohn MJ, Spear F (2000) Retrograde net transfer reaction insurance for pressure-temperature estimates. Geology 28:1127–1130

Kohn MJ, Malloy MA (2004) Formation of monazite via prograde metamorphic reactions among common silicates: implications for age determinations. Geochim Cosmochim Acta 68:101–113

Kohn MJ, Corrie SL, Markley C (2015) The fall and rise of metamorphic zircon. Am Mineral 100:897–908

Kohn (2017) Title of Chapter. Rev Mineral Geochem XX:xxx–xxx.

Korhonen F,J Brown M, Clark C, Bhattacharya S (2013a) Osumilite–melt interactions in ultrahigh temperature granulites: phase equilibria modelling and implications for the P–T–t evolution of the Eastern Ghats Province, India. J Metamorph Geol 31:881–907

Korhonen FJ, Clark C, Brown M, Bhattacharya S, Taylor R (2013b) How long-lived is ultrahigh temperature (UHT) metamorphism? Constraints from zircon and monazite geochronology in the Eastern Ghats orogenic belt, India. Precambrian Res 234:322–350

Korhonen FJ, Clark C, Brown M, Taylor RJM (2014) Taking the temperature of Earth's hottest crust. Earth Planet Sci Lett 408:341–354

Korhonen FJ, Brown M, Grove M, Siddoway CS, Baxter EF, Inglis JD (2012) Separating metamorphic events in the Fosdick migmatite–granite complex, West Antarctica. J Metamorph Geol 30:165–192

Kylander-Clark ARC, Hacker BR, Cottle JM (2013) Laser-ablation split-stream ICP petrochronology. Chem Geol 345:99–112

Lanari and Engi (2017) Title of Chapter. Rev Mineral Geochem XX:xxx–xxx.

Mahar EM, Baker JM, Powell R, Holland TJB, Howell N (1997) The effect of Mn on mineral stability in metapelites. J Metamorph Geol 15:223–238

Mayne MJ, Moyen JF, Stevens G, Kaisl Aniemi L (2016) Rcrust: a tool for calculating path‐dependent open system processes and application to melt loss. J Metamorph Geol 34: 663‐682.

McClelland WC, Lapen TJ (2013) Linking time to the pressure–temperature path for ultrahigh-pressure rocks. Elements 9:273–279

Mezger K, Hanson GN, Bohlen SR (1989) High-precision U–Pb ages of metamorphic rutile: application to the cooling history of high-grade terranes. Earth Planet Sci Lett 96:106-118

Miyazaki K (1991) Ostwald ripening of garnet in high P/T metamorphic rocks. Contr Mineral and Petrol 108:118–128

Miyazaki K (1996) A numerical simulation of textural evolution due to Ostwald ripening in metamorphic rocks: A case for small amount of volume of dispersed crystals. Geochim Cosmochim Acta 60:277–290

Molina JF, Moreno JA, Castro A, Rodríguez C, Fershtater GB (2015) Calcic amphibole thermobarometry in metamorphic and igneous rocks: New calibrations based on plagioclase/amphibole Al-Si partitioning and amphibole/liquid Mg partitioning. Lithos 232:286-305

Montel, J-M Kornprobst, J Vielzeuf, D (2000) Preservation of old U–Th–Pb ages in shielded monazite: example from the Beni Bousera Hercynian kinzigites (Morocco). J Metamorph Geol 18:335–342

Montel J-M (1986) Experimental determination of the solubility of Ce-monazite in SiO2-Al2O3-K2O-Na2O melts at 800 C, 2 kbar, under H2O-saturated conditions. Geology 14:659–662

Morrissey LJ, Hand M, Raimondo T, Kelsey DE (2014) Long-lived high-T, low-P granulite facies metamorphism in the Arunta Region, central Australia. J Metamorph Geol 32:25–47

Moynihan DP, Pattison DRM (2013) An automated method for the calculation of P–T paths from garnet zoning, with application to metapelitic schist from the Kootenay Arc, British Columbia, Canada. J Metamorph Geol 31:525–548

Mulcahy SR, Vervoort JD, Renne PR (2014) Dating subduction-zone metamorphism with combined garnet and lawsonite Lu–Hf geochronology. J Metamorph Geol 32:515–533

Nemchin AA, Bodorkos S (2000) Zr and LREE concentrations in anatectic melt as a function of crystal size distributions of zircon and monazite in the source region. Geological Society of America, Abstracts and Programs: 52286

Nemchin AA, Giannini LM, Bodorkos S, Oliver NHS (2001) Ostwald ripening as a possible mechanism for zircon overgrowth formation during anatexis: theoretical constraints, a numerical model, and its application to pelitic migmatites of the Tickalara Metamorphics, northwestern Australia. Geochim Cosmochim Acta 65:2771–2788

O'Brien PJ, Rötzler J (2003) High-pressure granulites: formation, recovery of peak conditions and implications for tectonics. J Metamorph Geol 21:3–20

Parrish RR (1990) U-Pb dating of monazite and its application to geological problems. Can J Earth Sci 27:1431–1450

Pattison DRM, Tinkham DK (2009) Interplay between equilibrium and kinetics in prograde metamorphism of pelites: an example from the Nelson aureole, British Columbia. J Metamorph Geol 27:249–279

Pattison DRM, DeBuhr CL (2015) Petrology of metapelites in the Bugaboo aureole, British Columbia, Canada. J Metamorph Geol 33:437-462

Pattison DRM, Chacko T, Farquhar J, McFarlane CRM (2003) Temperatures of granulite-facies metamorphism: constraints from experimental phase equilibria and thermobarometry corrected for retrograde exchange. J Petrol 44:867–900

Pichavant M, Montel J-M, Richard LR (1992) Apatite solubility in peraluminous liquids: Experimental data and an extension of the Harrison-Watson model. Geochim Cosmochim Acta 56:3855-3861

Powell R (1983) Processes in granulite-facies metamorphism. *In*: Proceedings of the Geochemical Group of the Mineraological Society: Migmatites, melting and metamorphism. Atherton, MP, Gribble, CD (eds). Shiva, Nantwich, p 127–139

Powell R, Holland TJB (1988) An internally consistent dataset with uncertainties and correlations: 3. Applications to geobarometry, worked examples and a computer program. J Metamorph Geol 6:173–204

Powell R, Holland TJB (2008) On thermobarometry. J Metamorph Geol 26:155–179

Powell R, Holland T, Worley B (1998) Calculating phase diagrams involving solid solutions via non-linear equations, with examples using THERMOCALC. J Metamorph Geol 16:577–588

Powell R, Guiraud M, White RW (2005) Truth and beauty in metamorphic phase-equilibria: conjugate variables and phase diagrams. Can Mineral 43:21–33

Pyle JM, Spear FS (1999) Yttrium zoning in garnet: coupling of major and accessory phases during metamorphic reactions. Geol Mat Res 1:1–49

Pyle JM, Spear FS (2000) An empirical garnet (YAG)–xenotime thermometer. Contr Mineral and Petrol 138:51–58

Pyle JM, Spear FS, Rudnick RL, McDonough WF (2001) Monazite–xenotime–garnet equilibrium in metapelites and a new monazite–garnet thermometer. J Petrol 42:2083–2107

Rapp RP, Watson EB (1986) Monazite solubility and dissolution kinetics: implications for the thorium and light rare earth chemistry of felsic magmas. Contr Mineral and Petrol 94:304–316

Rapp RP, Ryerson FJ, Miller CF (1987) Experimental evidence bearing on the stability of monazite during crustal anaatexis. Geophys Res Lett 14:307-310

Rasmussen B (2005) Radiometric dating of sedimentary rocks: the application of diagenetic xenotime geochronology. Earth Sci Rev 68:197-243

Rasmussen B, Muhling JR (2007) Monazite begets monazite: evidence for dissolution of detrital monazite and reprecipitation of syntectonic monazite during low-grade regional metamorphism. Contr Mineral and Petrol 154:675–689

Rasmussen B, Fletcher IR, Muhling JR (2011) Response of xenotime to prograde metamorphism. Contr Mineral and Petrol 162:1259–1277

Regis D, Warren CJ, Mottram CM, Roberts NMW (2016) Using monazite and zircon petrochronology to constrain the P–T–t evolution of the middle crust in the Bhutan Himalaya. J Metamorph Geol

Reno BL, Piccoli PM, Brown M, Trouw RAJ (2012) In situ monazite (U–Th)–Pb ages from the Southern Brasília Belt, Brazil: constraints on the high-temperature retrograde evolution of HP granulites. J Metamorph Geol 30:81–112

Roberts MP, Finger F (1997) Do U-Pb zircon ages from granulites reflect peak metamorphic conditions? Geology 25:319-322

Rocha BC, Moraes R, Möller A, Cioffi CR, Jercinovic MJ (2016) Timing of anatexis and melt crystallization in the Socorro–Guaxupé Nappe, SE Brazil: Insights from trace element composition of zircon, monazite and garnet coupled to U–Pb geochronology. Lithos

Rubatto (2017) Title of Chapter. Rev Mineral Geochem XX:xxx–xxx.

Rubatto D (2002) Zircon trace element geochemistry: partitioning with garnet and the link between U–Pb ages and metamorphism. Chem Geol 184:123–138

Rubatto D, Hermann J (2003) Zircon formation during fluid circulation in eclogites (Monviso, Western Alps): implications for Zr and Hf budget in subduction zones. Geochim Cosmochim Acta 67:2173–2187

Rubatto D, Hermann J (2007) Experimental zircon/melt and zircon/garnet trace element partitioning and implications for the geochronology of crustal rocks. Chem Geol 241:38–61

Rubatto D, Williams IS, Buick IS (2001) Zircon and monazite response to prograde metamorphism in the Reynolds Range, central Australia. Contr Mineral and Petrol 140:458–468

Rubatto D, Chakraborty S, Dasgupta S (2013) Timescales of crustal melting in the Higher Himalayan Crystallines (Sikkim, Eastern Himalaya) inferred from trace element-constrained monazite and zircon chronology. Contr Mineral and Petrol 165:349–372

Schaltegger U (2007) Hydrothermal zircon. Elements 3:51–79

Schaltegger U, Fanning CM, Günther D, Maurin JC, Schulmann K, Gebauer D (1999) Growth, annealing and recrystallization of zircon and preservation of monazite in high-grade metamorphism: conventional and in-situ U-Pb isotope, cathodoluminescence and microchemical evidence. Contr Mineral and Petrol 134:186-201

Sheppard S, Rasmussen B, Muhling JR, Farrell TR, Fletcher IR (2007) Grenvillian-aged orogenesis in the Palaeoproterozoic Gascoyne Complex, Western Australia: 1030-950 Ma reworking of the Proterozoic Capricorn Orogen. J Metamorph Geol 25:477-494

Shaw DM (1956) Geochemistry of pelitic rocks. Part III: Major elements and general geochemistry. Geol Soc Am Bull 67:919–934

Shazia JR, Harlov DE, Suzuki K, Kim SW, Girish-Kumar M, Hayasaka Y, Ishwar-Kumar C, Windley BF, Sajeev K (2015) Linking monazite geochronology with fluid infiltration and metamorphic histories: Nature and experiment. Lithos 236:1–15

Skora S, Blundy J (2012) Monazite solubility in hydrous silicic melts at high pressure conditions relevant to subduction zone metamorphism. Earth Planet Sci Lett 321:104–114

Sláma J, Košler J, Pedersen RB (2007) Behaviour of zircon in high-grade metamorphic rocks: evidence from Hf isotopes, trace elements and textural studies. Contr Mineral and Petrol 154:335–356

Smith HA, Barreiro B (1990) Monazite U-Pb dating of staurolite grade metamorphism in pelitic schists. Contr Mineral and Petrol 105:602–615

Smye AJ, Stockli DF (2014) Rutile U–Pb age depth profiling: A continuous record of lithospheric thermal evolution. Earth Planet Sci Lett 408:171–182

Spear FS (1995) Metamorphic phase equilibria and pressure-temperature-time paths. Mineralogical Society of America Washington

Spear FS (2010) Monazite–allanite phase relations in metapelites. Chem Geol 279:55-62

Spear FS, Florence FP (1992) Thermobarometry in granulites: pitfalls and new approaches. Precambrian Res 55:209–241

Spear FS, Pyle JM (2002) Apatite, monazite, and xenotime in metamorphic rocks. Rev Mineral Geochem 48:293–335

Spear FS, Pyle JM (2010) Theoretical modeling of monazite growth in a low-Ca metapelite. Chem Geol 273:111–119

Spear FS, Pattison DRM, Cheney JT (2016) The metamorphosis of metamorphic petrology. Geol Soc Am Sp Pap 523:SPE523-502

Spencer KJ, Hacker BR, Kylander-Clark ARC, Andersen TB, Cottle JM, Stearns MA, Poletti JE, Seward GGE (2013) Campaign-style titanite U–Pb dating by laser-ablation ICP: implications for crustal flow, phase transformations and titanite closure. Chem Geol 341:84–101

Stearns MA, Hacker BR, Ratschbacher L, Rutte D, Kylander-Clark ARC (2015) Titanite petrochronology of the Pamir gneiss domes: Implications for middle to deep crust exhumation and titanite closure to Pb and Zr diffusion. Tectonics 34:784–802

Stepanov AS, Hermann J, Rubatto D, Rapp RP (2012) Experimental study of monazite/melt partitioning with implications for the REE, Th and U geochemistry of crustal rocks. Chem Geol 300:200–220

Štípská P, Hacker BR, Racek M, Holder R, Kylander-Clark ARC, Schulmann K, Hasalová P (2015) Monazite Dating of Prograde and Retrograde P–T–d paths in the Barrovian terrane of the Thaya window, Bohemian Massif. J Petrol 56:1007–1035

Stüwe K (1997) Effective bulk composition changes due to cooling: a model predicting complexities in retrograde reaction textures. Contr Mineral and Petrol 129:43–52

Stüwe K, Powell R (1995) PT paths from modal proportions: application to the Koralm Complex, Eastern Alps. Contr Mineral and Petrol 119:83–93

Sun S-S, McDonough W (1989) Chemical and isotopic systematics of oceanic basalts: implications for mantle composition and processes. Geol Soc London, Sp Pub 42:313–345

Suzuki K, Adachi M (1994) Middle Precambrian detrital monazite and zircon from the Hida gneiss on Oki-Dogo Island, Japan: their origin and implications for the correlation of basement gneiss of Southwest Japan and Korea. Tectonophysics 235:277–292

Symmes GH, Ferry JM (1992) The effect of whole-rock MnO content on the stability of garnet in pelitic schists during metamorphism. J Metamorph Geol 10:221–237

Taylor RJM, Clark C, Fitzsimons ICW, Santosh M, Hand M, Evans N, McDonald B (2014) Post-peak, fluid-mediated modification of granulite facies zircon and monazite in the Trivandrum Block, southern India. Contr Mineral and Petrol 168:1–17

Taylor RJM, Harley SL, Hinton RW, Elphick S, Clark C, Kelly NM (2015) Experimental determination of REE partition coefficients between zircon, garnet and melt: a key to understanding high-T crustal processes. J Metamorph Geol 33:231–248

Taylor-Jones K, Powell R (2015) Interpreting zirconium-in-rutile thermometric results. J Metamorph Geol 33:115–122

Thompson AB (1982) Dehydration melting of pelitic rocks and the generation of H_2O-undersaturated granitic liquids. Am J Sci 282:1567–1595

Thompson AB (1996) Fertility of crustal rocks during anatexis. Geol Soc Am Sp Pap 315:1–10

Thompson AB, England PC (1984) Pressure—temperature—time paths of regional metamorphism II. Their inference and interpretation using mineral assemblages in metamorphic rocks. J Petrol 25:929–955

Tikare V, Cawley JD (1998) Application of the Potts model to simulation of Ostwald ripening. J Am Ceram Soc 81:485–491

Tomaschek F, Kennedy AK, Villa IM, Lagos M, Ballhaus C (2003) Zircons from Syros, Cyclades, Greece—recrystallization and mobilization of zircon during high-pressure metamorphism. J Petrol 44:1977–2002

Tomkins HS, Powell R, Ellis DJ (2007) The pressure dependence of the zirconium-in-rutile thermometer. J Metamorph Geol 25:703–713

Vance D, O'Nions RK (1990) Isotopic chronometry of zoned garnets: growth kinetics and metamorphic histories. Earth Planet Sci Lett 97:227–240

Vance D, Mahar E (1998) Pressure-temperature paths from PT pseudosections and zoned garnets: potential, limitations and examples from the Zanskar Himalaya, NW India. Contr Mineral and Petrol 132:225–245

Vavra G, Schmid R, Gebauer D (1999) Internal morphology, habit and U-Th-Pb microanalysis of amphibolite-to-granulite facies zircons: geochronology of the Ivrea Zone (Southern Alps). Contr Mineral and Petrol 134:380–404

Vernon RH (1996) Problems with inferring P-T-t paths in low-P granulite facies rocks. J Metamorph Geol 14:143–153

Vielzeuf D, Schmidt MW (2001) Melting relations in hydrous systems revisited: application to metapelites, metagreywackes and metabasalts. Contr Mineral and Petrol 141:251–267

Walsh AK, Kelsey DE, Kirkland CL, Hand M, Smithies RH, Clark C, Howard HM (2015) P–T–t evolution of a large, long-lived, ultrahigh-temperature Grenvillian belt in central Australia. Gondwana Res 28:531–564

Wark DA, Watson EB (2006) TitaniQ: a titanium-in-quartz geothermometer. Contr Mineral and Petrol 152:743–754

Warren CJ, Grujic D, Cottle JM, Rogers NW (2012) Constraining cooling histories: rutile and titanite chronology and diffusion modelling in NW Bhutan. J Metamorph Geol 30:113–130

Watson EB (1996) Dissolution, growth and survival of zircons during crustal fusion: kinetic principles, geological models and implications for isotopic inheritance. Geol Soc Am Sp Pap 315:43–56

Watson EB, Harrison TM (1983) Zircon saturation revisited: temperature and composition effects in a variety of crustal magma types. Earth Planet Sci Lett 64:295–304

Watson EB, Vicenzi EP, Rapp RP (1989) Inclusion/host relations involving accessory minerals in high-grade metamorphic and anatectic rocks. Contr Mineral and Petrol 101:220–231

Watson EB, Wark DA, Thomas JB (2006) Crystallization thermometers for zircon and rutile. Contr Mineral and Petrol 151:413-433

Watt GR, Harley SL (1993) Accessory phase controls on the geochemistry of crustal melts and restites produced during water-undersaturated partial melting. Contr Mineral and Petrol 114:550–566

White RW, Powell R (2002) Melt loss and the preservation of granulite facies mineral assemblages. J Metamorph Geol 20:621–632

White RW, Powell R, Halpin JA (2004) Spatially-focussed melt formation in aluminous metapelites from Broken Hill, Australia. J Metamorph Geol 22:825–845

White RW, Pomroy NE, Powell R (2005) An in situ metatexite–diatexite transition in upper amphibolite facies rocks from Broken Hill, Australia. J Metamorph Geol 23:579–602

White RW, Powell R, Johnson TE (2014a) The effect of Mn on mineral stability in metapelites revisited: New a‑x relations for manganese-bearing minerals. J Metamorph Geol 32:809–828

White RW, Powell R, Baldwin JA (2008) Calculated phase equilibria involving chemical potentials to investigate the textural evolution of metamorphic rocks. J Metamorph Geol 26:181–198

White RW, Stevens G, Johnson TE (2011) Is the crucible reproducible? Reconciling melting experiments with thermodynamic calculations. Elements 7:241–246

White RW, Powell R, Holland TJB, Johnson TE, Green ECR (2014b) New mineral activity–composition relations for thermodynamic calculations in metapelitic systems. J Metamorph Geol 32:261–286

White WM, Klein EM (2014) 4.13 - Composition of the Oceanic Crust. *In*: Treatise on Geochemsitry (Second Edition). Holland, HD, Turekian, K (ed). Elsevier, Oxford, p 457–496

Williams ML, Jercinovic MJ, Harlov DE, Budzyń B, Hetherington CJ (2011) Resetting monazite ages during fluid-related alteration. Chem Geol 283:218–225

Wing BA, Ferry JM, Harrison TM (2003) Prograde destruction and formation of monazite and allanite during contact and regional metamorphism of pelites: petrology and geochronology. Contr Mineral and Petrol 145:228–250

Wolf MB, London D (1994) Apatite dissolution into peraluminous haplogranitic melts: an experimental study of solubilities and mechanisms. Geochim Cosmochim Acta 58:4127–4145

Wolf MB, London D (1995) Incongruent dissolution of REE-and Sr-rich apatite in peraluminous granitic liquids: Differential apatite, monazite, and xenotime solubilities during anatexis. Am Mineral 80:765–775

Worley B, Powell R (1998) Making movies: phase diagrams changing in pressure, temperature, composition and time. Geol Soc London, Sp Pub 138:269-280

Wu CM (2015) Revised empirical garnet–biotite–muscovite–plagioclase geobarometer in metapelites. J Metamorph Geol 33:167–176

Xu H, Ye K, Song Y, Chen Y, Zhang J, Liu Q, Guo S (2013) Prograde metamorphism, decompressional partial melting and subsequent melt fractional crystallization in the Weihai migmatitic gneisses, Sulu UHP terrane, eastern China. Chem Geol 341:16–37

Yakymchuk C, Brown M (2014a) Consequences of open-system melting in tectonics. J Geol Soc London 171:21–40

Yakymchuk C, Brown M (2014b) Behaviour of zircon and monazite during crustal melting. J Geol Soc London 171:465–479

Yakymchuk C, Brown M, Clark C, Korhonen FJ, Piccoli PM, Siddoway CS, Taylor RJM, Vervoort JD (2015) Decoding polyphase migmatites using geochronology and phase equilibria modelling. J Metamorph Geol 33:203–230

Yardley BWD, Valley JW (1997) The petrologic case for a dry lower crust. J Geophys Res B: Solid Earth 102:12173–12185

Zack T, Moraes R, Kronz A (2004) Temperature dependence of Zr in rutile: empirical calibration of a rutile thermometer. Contr Mineral and Petrol 148:471–488

Zack T, Stockli DF, Luvizotto GL, Barth MG, Belousova E, Wolfe MR, Hinton RW (2011) In situ U–Pb rutile dating by LA-ICP-MS: 208Pb correction and prospects for geological applications. Contr Mineral and Petrol 162:515-530

Zack (2017). Title of Chapter. Rev Mineral Geochem XX:xxx–xxx.

Zuluaga CA, Stowell HH, Tinkham DK (2005) The effect of zoned garnet on metapelite pseudosection topology and calculated metamorphic PT paths. Am Mineral 90:1619–1628

Figure Captions

Figure 1. Underestimation of metamorphic temperature when the bulk rock value of a_{TiO2} is less than 1.0 (the true value is shown by the contours), but a value of 1.0 is assumed in: (a) the Ti-in-quartz thermometer of Wark and Watson (2006), and (b) the Ti-in-zircon thermometer of Ferry and Watson (2007).

Figure 2. Compilation of the range of allanite to monazite reaction temperatures for variable bulk rock pelite compositions. Curves are from Spear (2010).

Figure 3. *P*–*T* pseudosection for the subsolidus metapelite. The solidus is shown by the heavy dashed line.

Figure 4. (a) Mode-box diagram and a_{TiO2} for the subsolidus clockwise *P*–*T* path for the metapelite. (b) Mode-box diagram and a_{TiO2} for the subsolidus hairpin *P*–*T* path.

Figure 5. *P*–*T* pseudosection for the subsolidus greywacke. The solidus is shown by the heavy dashed line.

Figure 6. (a) Mode-box diagram and a_{TiO2} for the subsolidus clockwise *P–T* path for the greywacke composition. (b) Mode-box diagram and a_{TiO2} for the subsolidus hairpin *P–T* path.

Figure 7. *P–T* pseudosection for suprasolidus metapelite. The solidus is shown by the heavy dashed line.

Figure 8. (a) Mode-box diagram and a_{TiO2} for the suprasolidus clockwise *P–T* path for the metapelite. (b) Amount of zircon and monazite remaining relative to the amount at the solidus and the ASI value of melt. (c) Mode-box diagram and a_{TiO2} for the counterclockwise *P–T* path for the metapelite. (d) Amount of zircon and monazite remaining relative to the amount at the solidus for the counterclockwise *P–T* path.

Figure 9. *P–T* pseudosection for the suprasolidus greywacke. The solidus is shown by the heavy dashed line.

Figure 10. (a) Mode-box diagram and a_{TiO2} for the suprasolidus clockwise *P–T* path for the greywacke. (b) Amount of zircon and monazite remaining relative to the amount at the solidus and the ASI value of melt. (c) Mode-box diagram and a_{TiO2} for the counterclockwise *P–T* path for the greywacke. (d) Amount of zircon and monazite remaining relative to the amount at the solidus for the counterclockwise *P–T* path.

Figure 11. *P–T* pseudosection for the suprasolidus MORB. The solidus is shown by the heavy dashed line.

Figure 12. (a) Mode-box diagram and a_{TiO2} for the suprasolidus clockwise *P–T* path for the MORB. (b) Amount of zircon remaining relative to the amount at the solidus and the ASI value of melt.

Figure 13. (a) *T–X* pseudosection calculated at 7 kbar showing the change in mineral assemblages for compositions ranging from the metapelite (left side) to the greywacke (right side). (b) *T–X* diagram with melt isopleths (mol%). (c) *T–X* diagram with the calculated amount of zircon dissolution assuming a bulk Zr concentration of 150 ppm. (d) Calculated amount of monazite dissolution assuming a bulk LREE concentration of 150 ppm. (e) *T–X* diagram with contours for the complete dissolution of zircon for a range of bulk rock Zr concentrations. (f) *T–X* diagram with contours for the complete dissolution of monazite for a range of bulk rock LREE concentrations.

Table 1. Bulk compositions used for phase equilibria modelling (mol%)

	Figures	**H_2O**	**SiO_2**	**Al_2O_3**	**CaO**	**MgO**	**FeO**	**K_2O**	**Na_2O**	**TiO_2**	**MnO**	**O**
subsolidus												
metapelite	3,4	+	64.58	13.65	1.59	5.53	8.03	2.94	2.00	0.91	0.17	0.60
greywacke	5,6	+	77.62	8.20	1.15	3.85	4.21	1.26	2.85	0.52	0.35	0.32
suprasolidus												
metapelite	7,8,13	6.24	60.55	12.80	1.49	5.18	7.52	2.76	1.88	0.85	0.16	0.60
greywacke	9,10,13	2.61	75.35	7.96	1.12	3.74	4.09	1.22	2.77	0.51	0.34	0.31
MORB	11,12	6.19	42.58	10.45	12.27	14.76	9.68	0.22	2.62	0.66	–	0.58

+ H_2O in excess, – not considered

(a) Ti-in-quartz thermometer

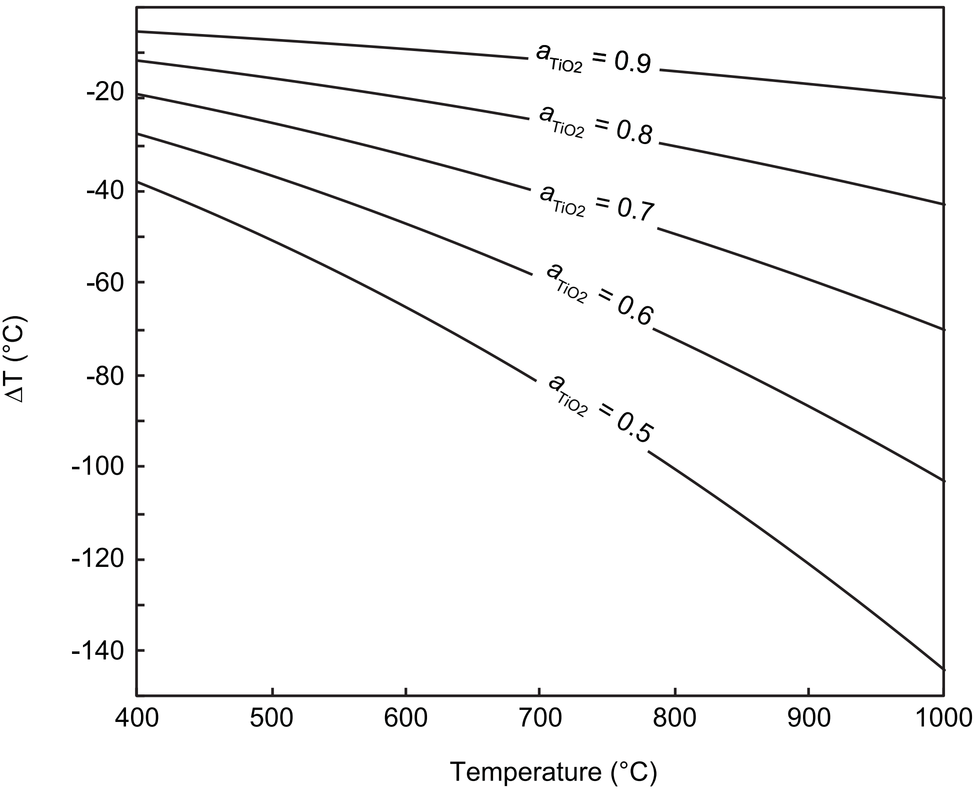

(b) Ti-in-zircon thermometer

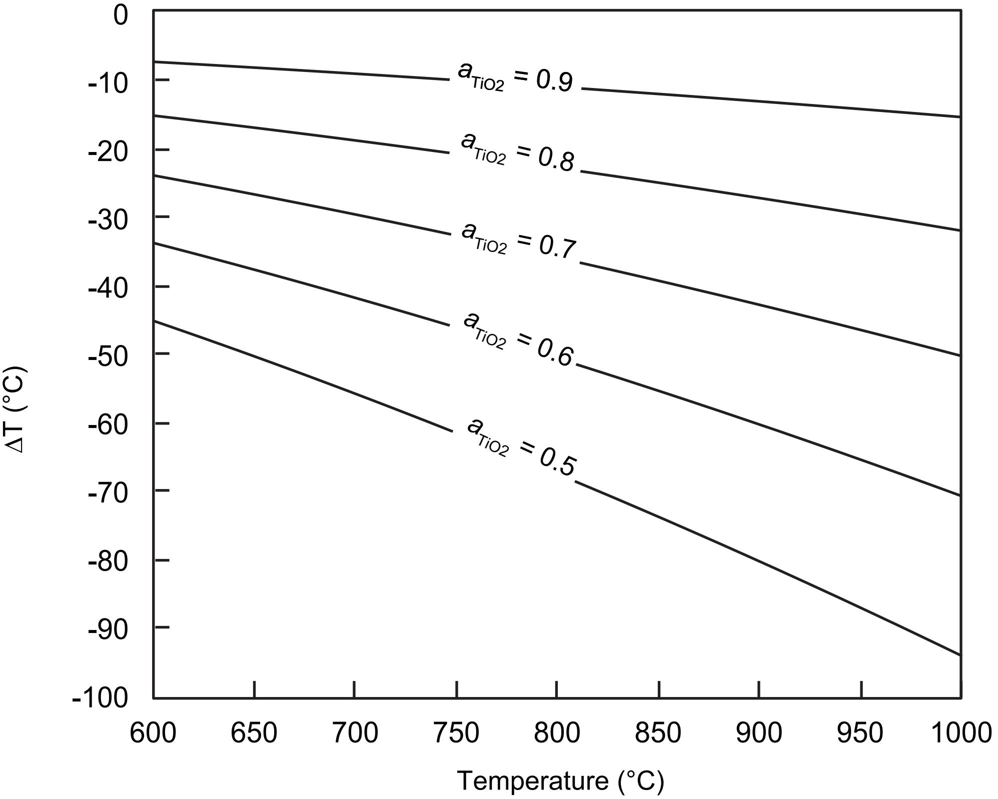

Figure 1

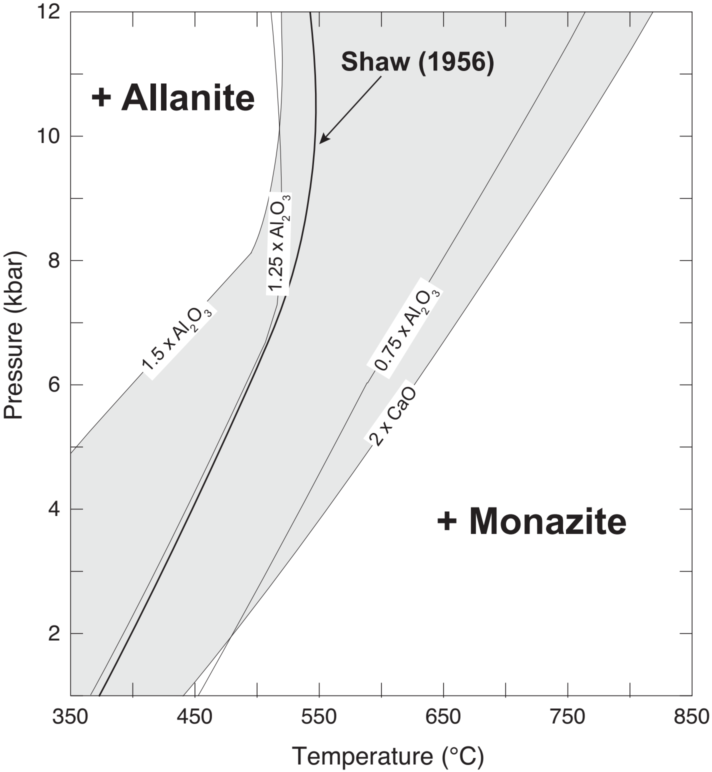

+ Allanite
+ Monazite
Shaw (1956)
1.5 x Al_2O_3
1.25 x Al_2O_3
0.75 x Al_2O_3
2 x CaO
Pressure (kbar)
12
10
8
6
4
2
350
450
550
650
750
850
Temperature (°C)

Figure 2

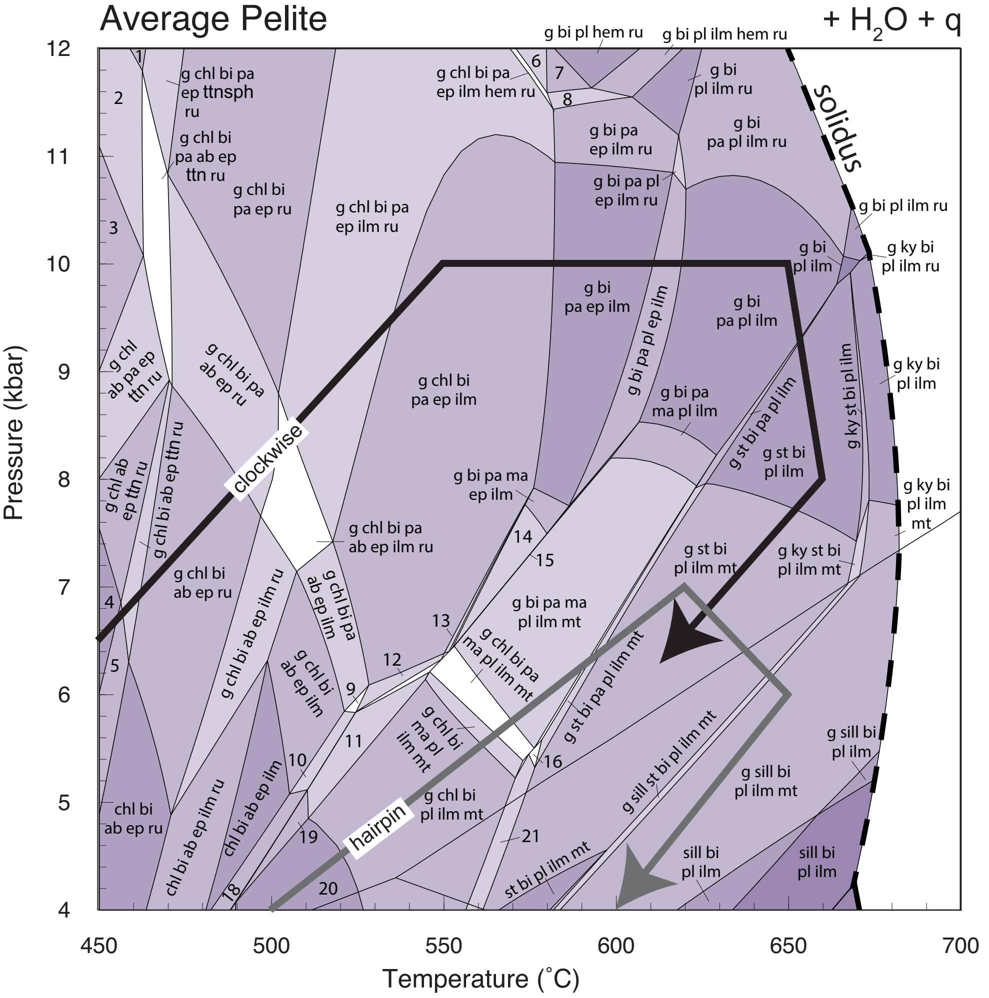

1) g chl bi pa ep ttn
2) g chl bi pa ab ep ttn
3) g chl pa ab ep ttn
4) chl ab ep ttn ru
5) chl bi ab ep ttn ru
6) g chl bi pa ep hem ru
7) g bi pa ep hem ru
8) g bi pa ep ilm hem ru
9) g chl bi pa pl ab ep ilm
10) g chl bi pl ab ep ilm
11) g chl bi pl ep ilm mt
12) g chl bi pa pl ep ilm
13) g chl bi pa ma ep ilm
14) g bi pa ma ep ilm mt
15) g bi pa ma pl ep ilm mt
16) g st chl bi pa pl ilm mt
17) chl bi pl ab ep ilm ru
18) chl bi pl ab ep ilm
19) chl bi pl ep ilm mt
20) chl bi pl ilm mt
21) g st chl bi pl ilm mt

Figure 3

(a) Metapelite: clockwise P–T

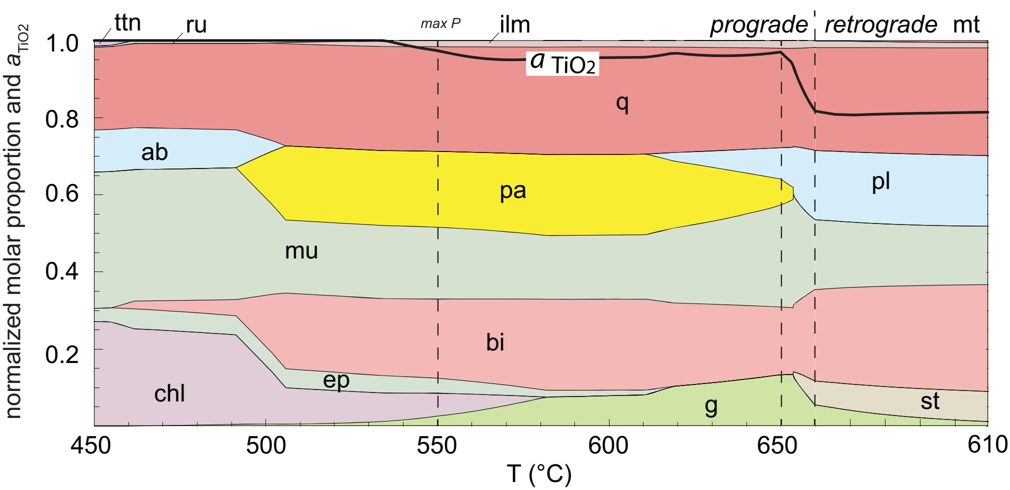

(b) Metapelite: hairpin P–T

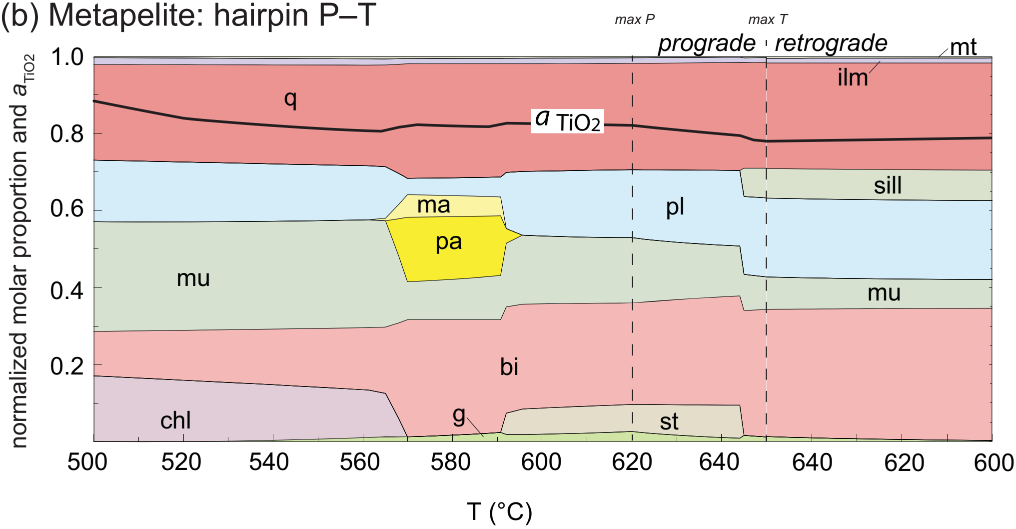

Figure 4.

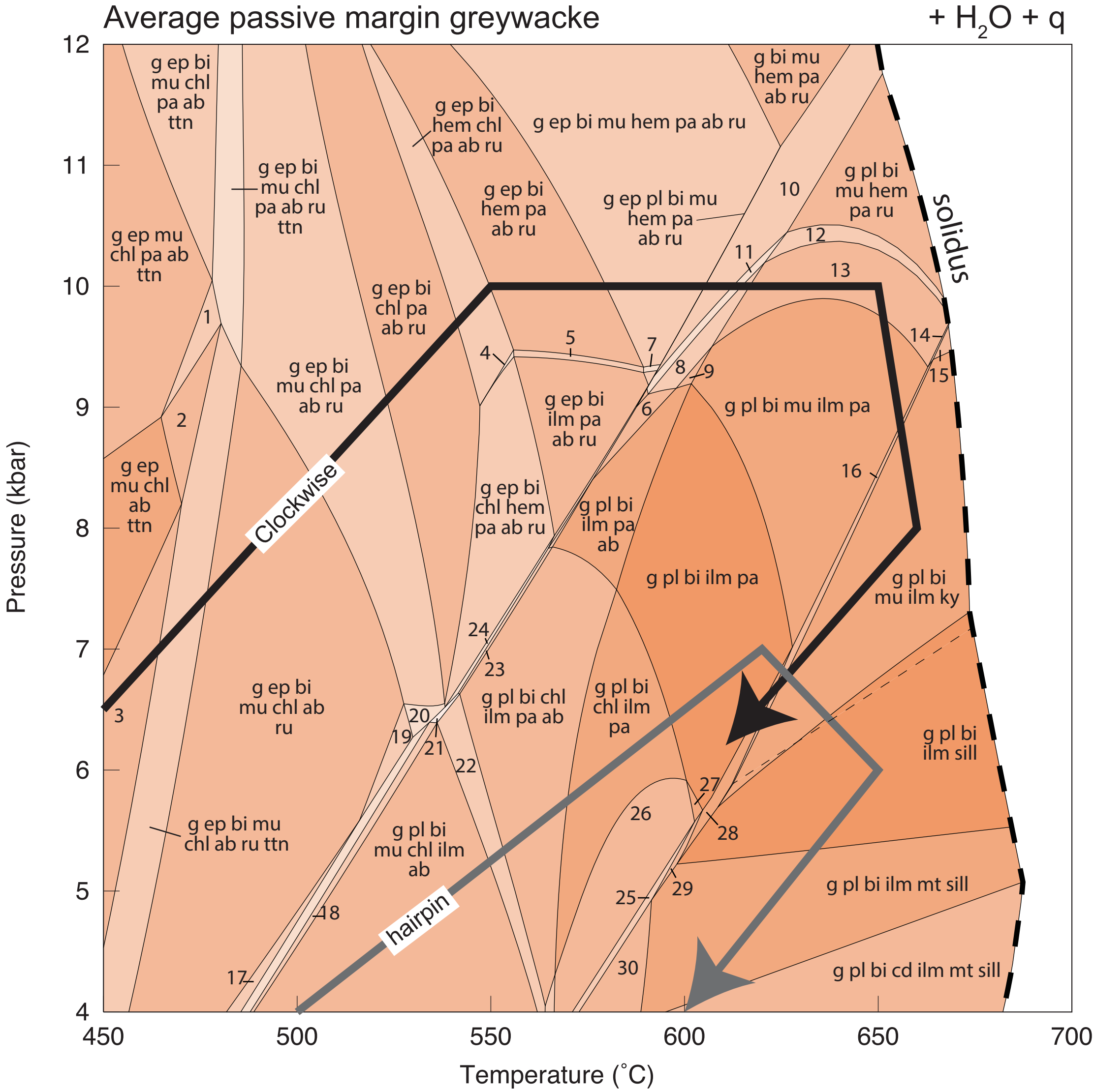

1. g ep mu chl pa ab ru ttn
2. g ep mu chl ab ru ttn
3. g ep bi mu chl ab ttn
4. g ep bi chl ilm hem pa ab ru
5. g ep bi ilm hem pa ab ru
6. g pl bi ilm pa ab ru
7. g ep pl bi mu ilm hem pa ab ru
8. g pl bi mu ilm pa ab ru
9. g pl bi mu ilm pa ab
10. g pl bi mu hem pa ab ru
11. g pl bi mu ilm hem pa ab ru
12. g pl bi mu ilm hem pa ru
13. g pl bi mu ilm pa ru
14. g pl bi mu ilm pa ru ky
15. g pl bi mu ilm ru ky
16. g pl bi mu ilm pa ky
17. g pl ep bi mu chl ab ru
18. g pl ep bi mu chl ilm ab
19. g ep bi mu chl ilm ab ru
20. g ep bi mu chl ilm pa ab ru
21. g pl ep bi mu chl ilm pa ab ru
22. g pl bi mu chl ilm pa ab
23. g pl ep bi chl ilm pa ab
24. g pl ep bi chl ilm pa ab ru
25. g pl bi chl ilm pa mt sill
26. g pl bi chl ilm pa mt
27. g pl bi ilm pa mt
28. g pl bi ilm pa sill
29. g pl bi ilm pa mt sill
30. g pl bi chl ilm mt sill

Figure 5

(a) Greywacke: clockwise P–T

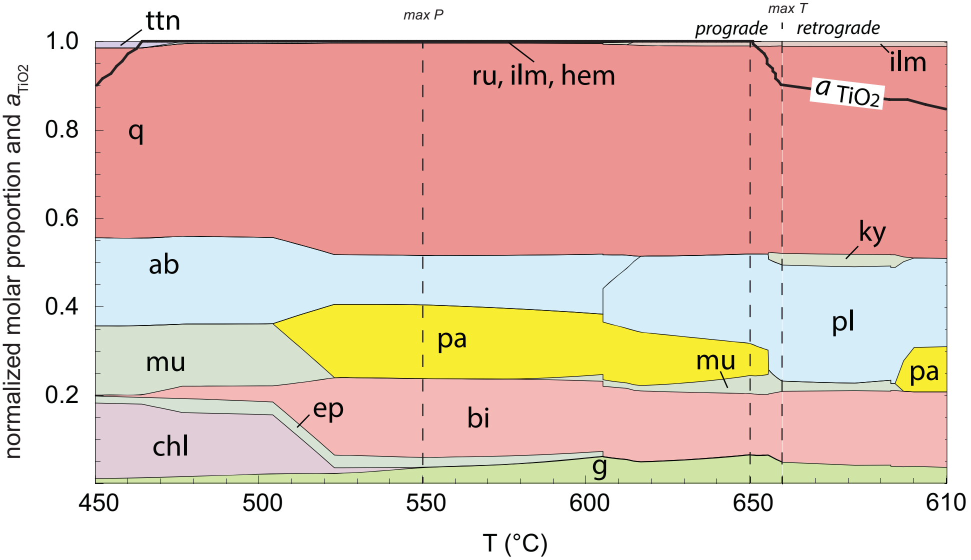

(b) Greywacke: hairpin P–T

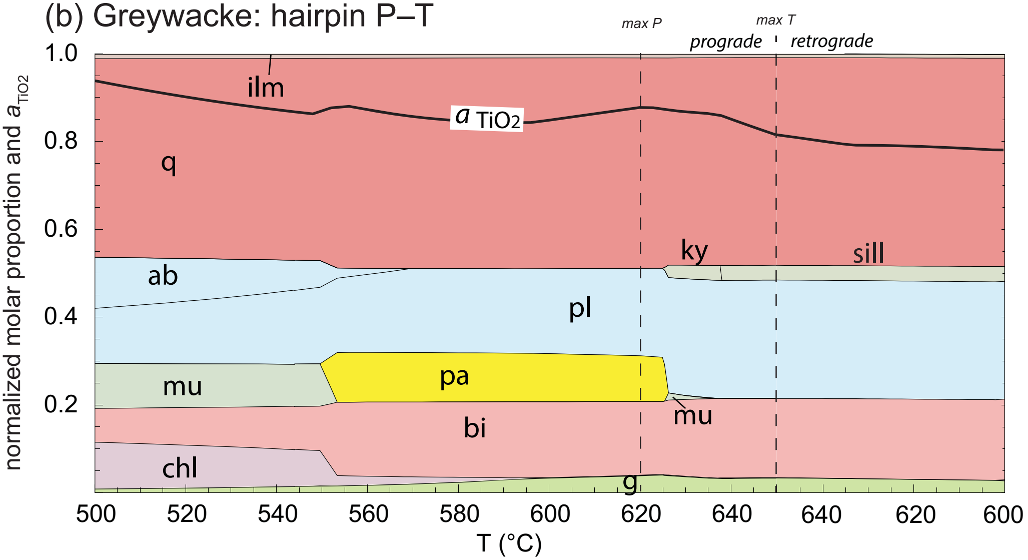

Figure 6

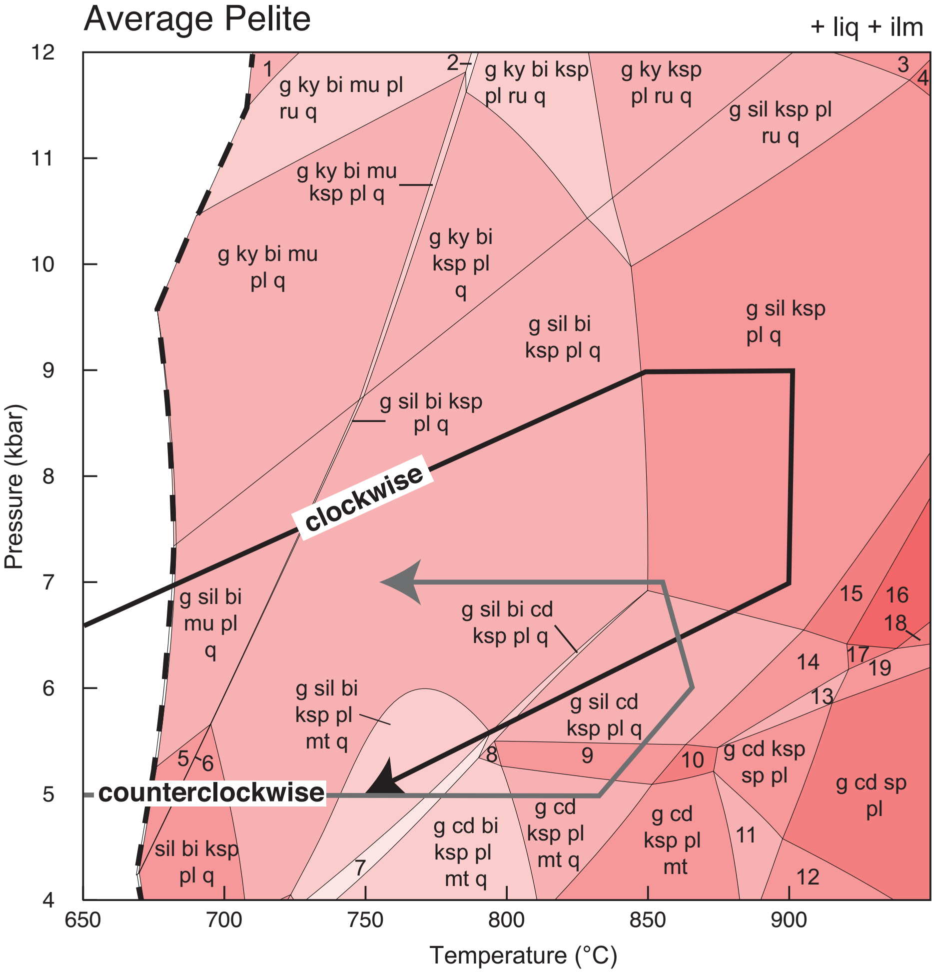

1: g bi bi mu pl ru q
2: g ky bi mu ksp pl ru q
3: g sil ksp ru q
4: g sil ksp q
5: sil bi mu pl q
6: sil ksp bi mu pl q
7: g sil cd bi ksp pl mt q

8: g cd bi ksp pl q
9: g cd ksp pl ru q
10: g cd ksp pl ru
11: g cd ksp sp pl mt
12: g cd sp pl mt
13: g sil cd ksp sp pl
14: g sil cd ksp pl

15: g sil ksp pl
16: g sil pl
17: g sil cd pl
18: g sil sp pl
19: g sil cd sp pl

Figure 7

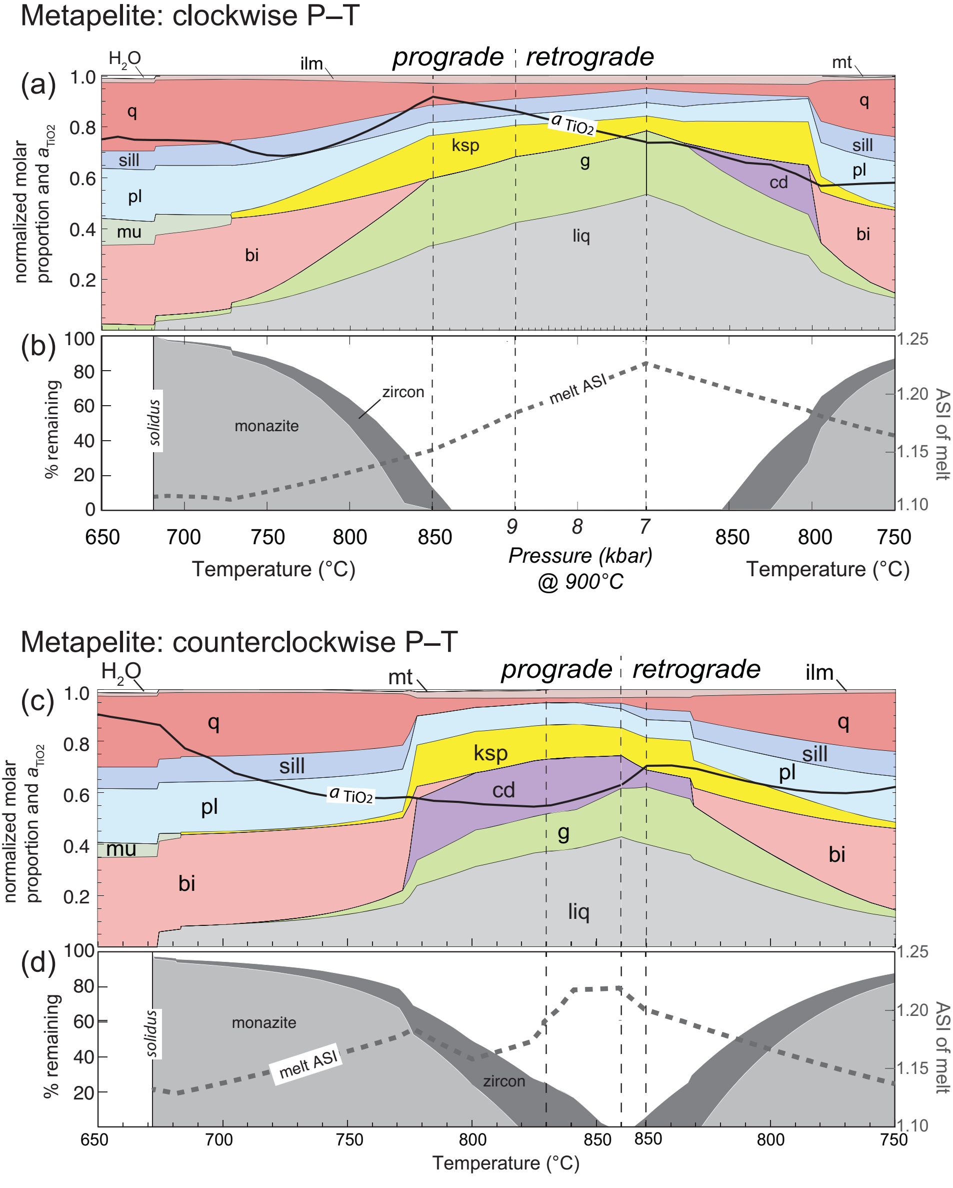
Metapelite: clockwise P–T
(a)
H2O
ilm
prograde
retrograde
mt
1.0
0.8
0.6
0.4
0.2
normalized molar proportion and aTiO2
q
sill
pl
mu
bi
ksp
a TiO2
g
liq
cd
(b)
100
80
60
40
20
0
% remaining
solidus
monazite
zircon
melt ASI
1.25
1.20
1.15
1.10
ASI of melt
650
700
750
800
850
9
8
7
850
800
750
Temperature (°C)
Pressure (kbar) @ 900°C
Temperature (°C)
Metapelite: counterclockwise P–T
(c)
H2O
mt
prograde
retrograde
ilm
1.0
0.8
0.6
0.4
0.2
normalized molar proportion and aTiO2
q
sill
pl
mu
bi
a TiO2
ksp
cd
g
liq
(d)
100
80
60
40
20
% remaining
solidus
monazite
melt ASI
zircon
1.25
1.20
1.15
1.10
ASI of melt
650
700
750
800
850
850
800
750
Temperature (°C)

Figure 8

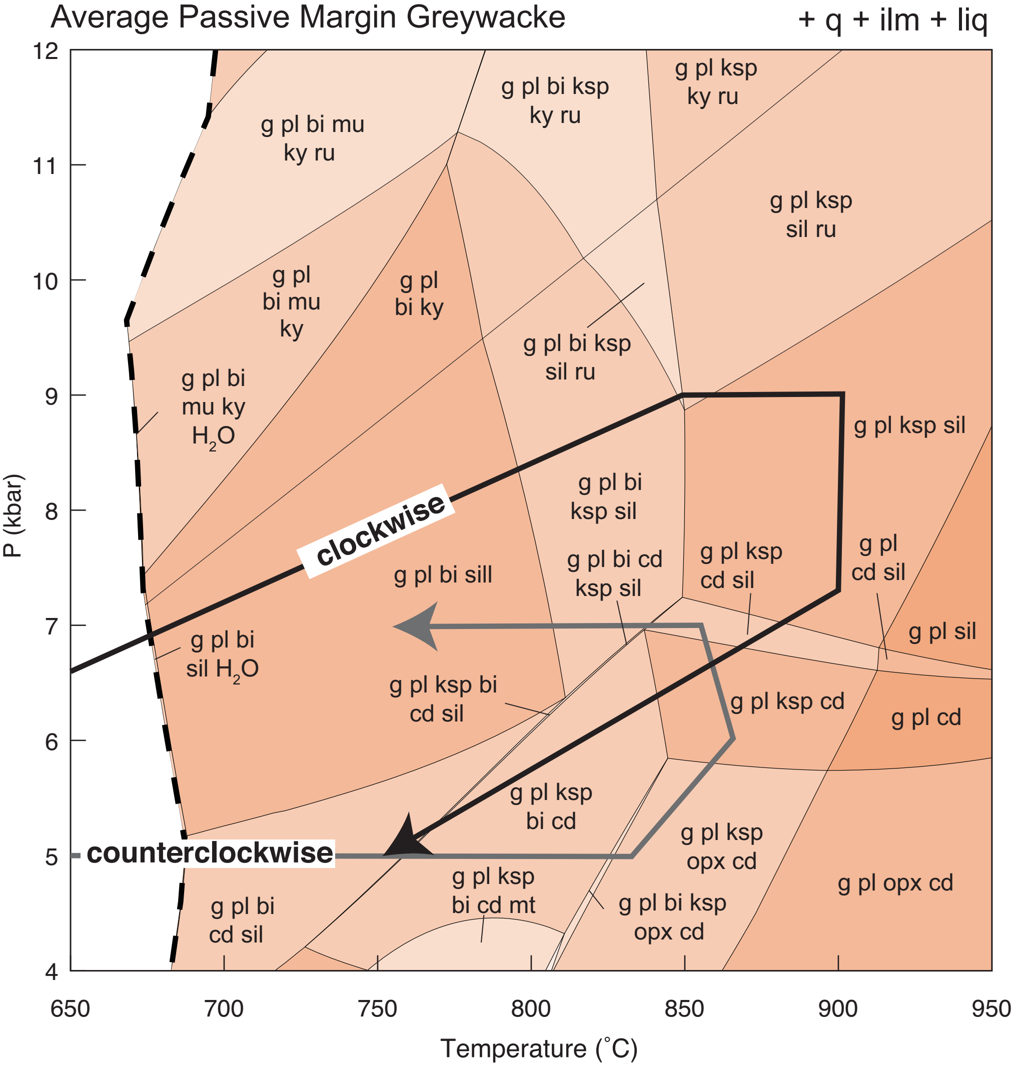
Average Passive Margin Greywacke
+ q + ilm + liq
P (kbar)
Temperature (˚C)
650
700
750
800
850
900
950
4
5
6
7
8
9
10
11
12
g pl bi mu ky ru
g pl bi ksp ky ru
g pl ksp ky ru
g pl ksp sil ru
g pl bi mu ky
g pl bi ky
g pl bi ksp sil ru
g pl bi mu ky H₂O
g pl ksp sil
g pl bi ksp sil
clockwise
g pl bi sill
g pl bi cd ksp sil
g pl ksp cd sil
g pl cd sil
g pl sil
g pl bi sil H₂O
g pl ksp bi cd sil
g pl ksp cd
g pl cd
g pl ksp bi cd
counterclockwise
g pl ksp opx cd
g pl opx cd
g pl bi cd sil
g pl ksp bi cd mt
g pl bi ksp opx cd

Figure 9

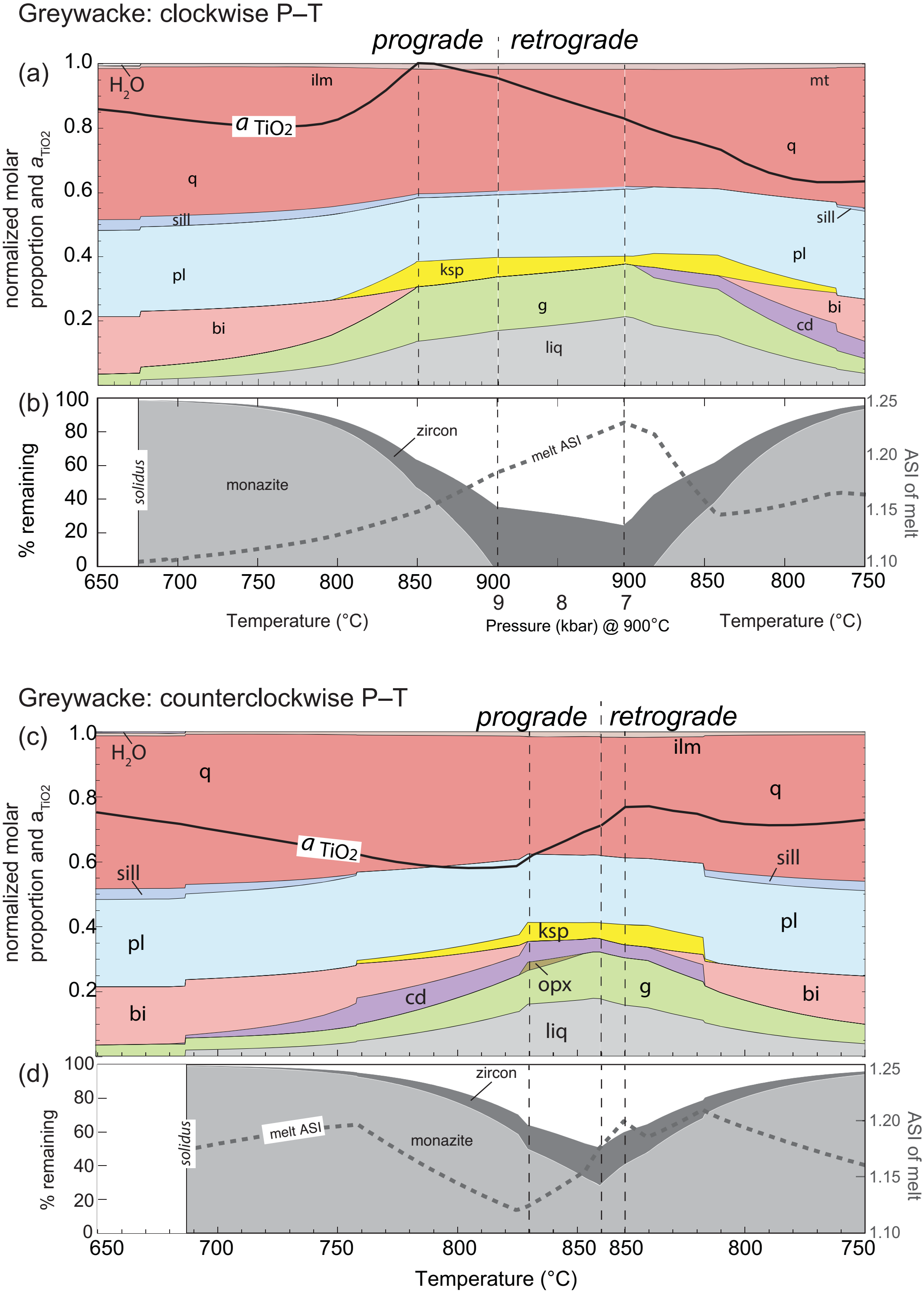
Greywacke: clockwise P–T
prograde
retrograde
(a)
1.0
0.8
0.6
0.4
0.2
normalized molar proportion and a_{TiO2}
H_2O
ilm
mt
a TiO2
q
q
sill
sill
pl
pl
ksp
g
bi
bi
cd
liq
(b)
100
80
60
40
20
0
% remaining
solidus
monazite
zircon
melt ASI
1.25
1.20
1.15
1.10
ASI of melt
650
700
750
800
850
900
900
850
800
750
9
8
7
Temperature (°C)
Pressure (kbar) @ 900°C
Temperature (°C)
Greywacke: counterclockwise P–T
prograde
retrograde
(c)
1.0
0.8
0.6
0.4
0.2
normalized molar proportion and a_{TiO2}
H_2O
ilm
q
q
a TiO2
sill
sill
pl
pl
ksp
opx
cd
g
bi
bi
liq
(d)
100
80
60
40
20
0
% remaining
solidus
zircon
melt ASI
monazite
1.25
1.20
1.15
1.10
ASI of melt
650
700
750
800
850
850
800
750
Temperature (°C)

Figure 10

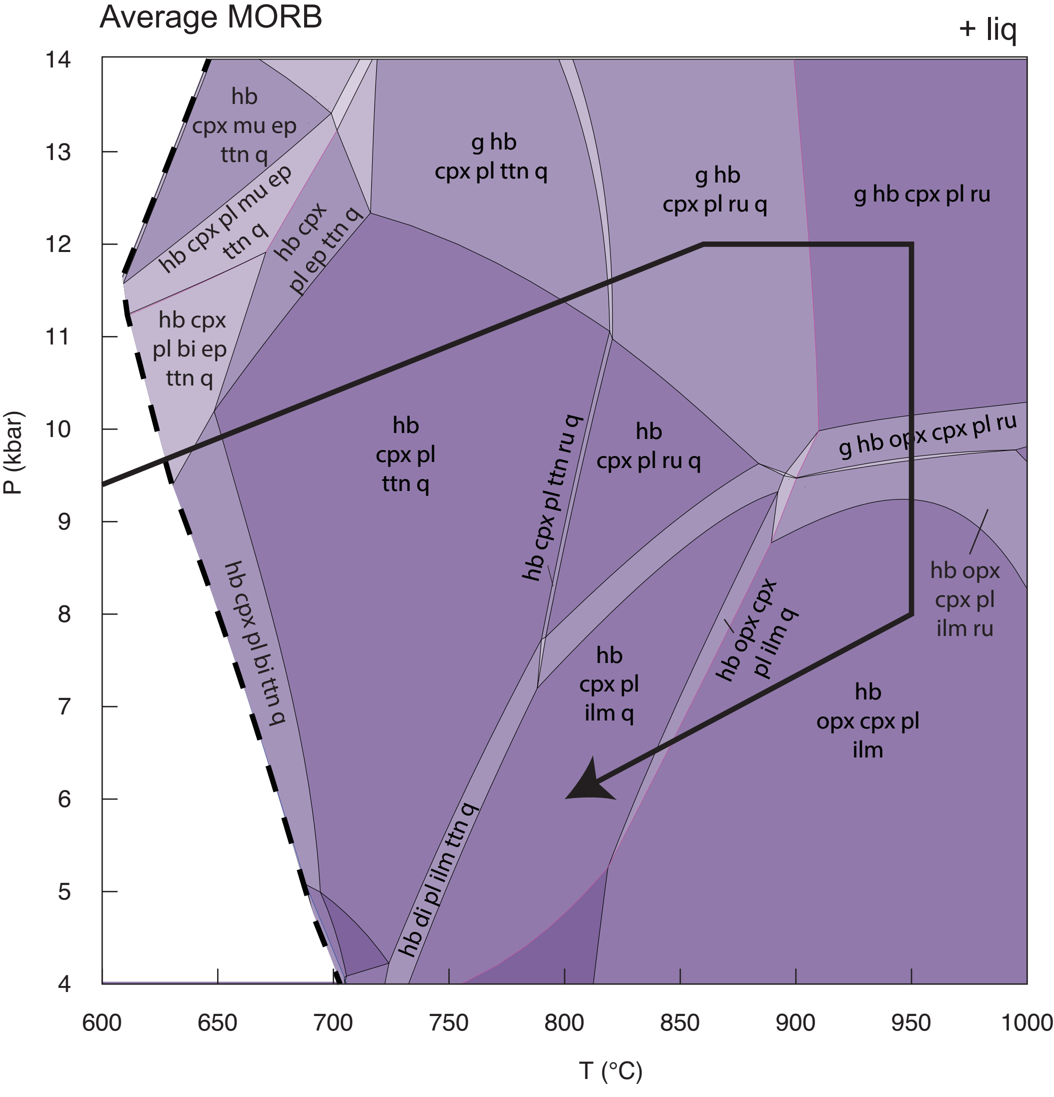
Average MORB
+ liq
hb cpx mu ep ttn q
hb cpx pl mu ep ttn q
hb cpx pl ep ttn q
hb cpx pl bi ep ttn q
g hb cpx pl ttn q
g hb cpx pl ru q
g hb cpx pl ru
g hb opx cpx pl ru
hb cpx pl ttn q
hb cpx pl ttn ru q
hb cpx pl ru q
hb cpx pl bi ttn q
hb cpx pl ilm q
hb opx cpx pl ilm q
hb opx cpx pl ilm ru
hb opx cpx pl ilm
hb di pl ilm ttn q
P (kbar)
14
13
12
11
10
9
8
7
6
5
4
600
650
700
750
800
850
900
950
1000
T (°C)

Figure 11

MORB: clockwise P–T

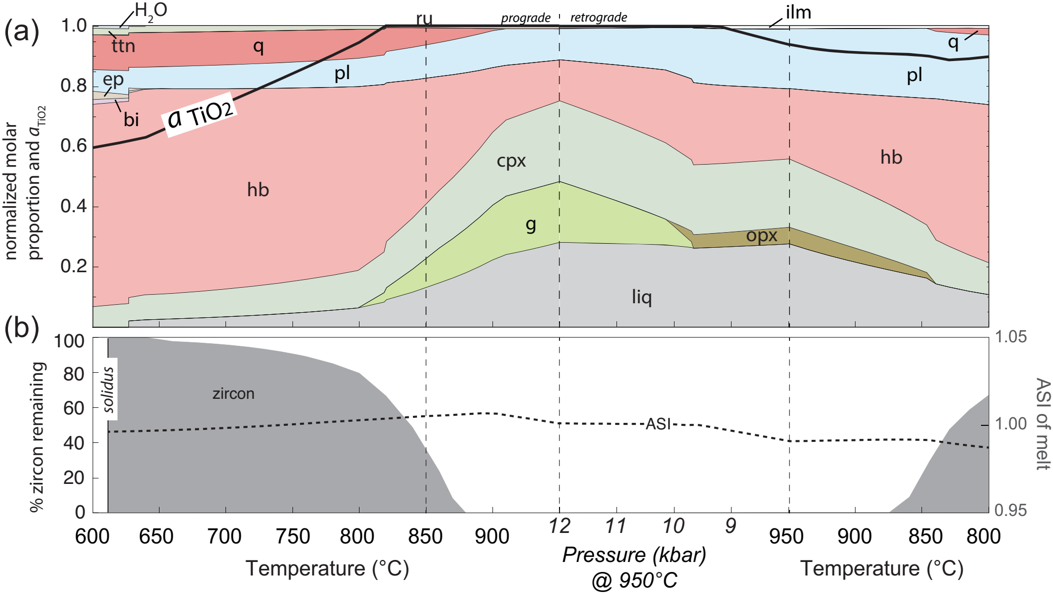

Figure 12

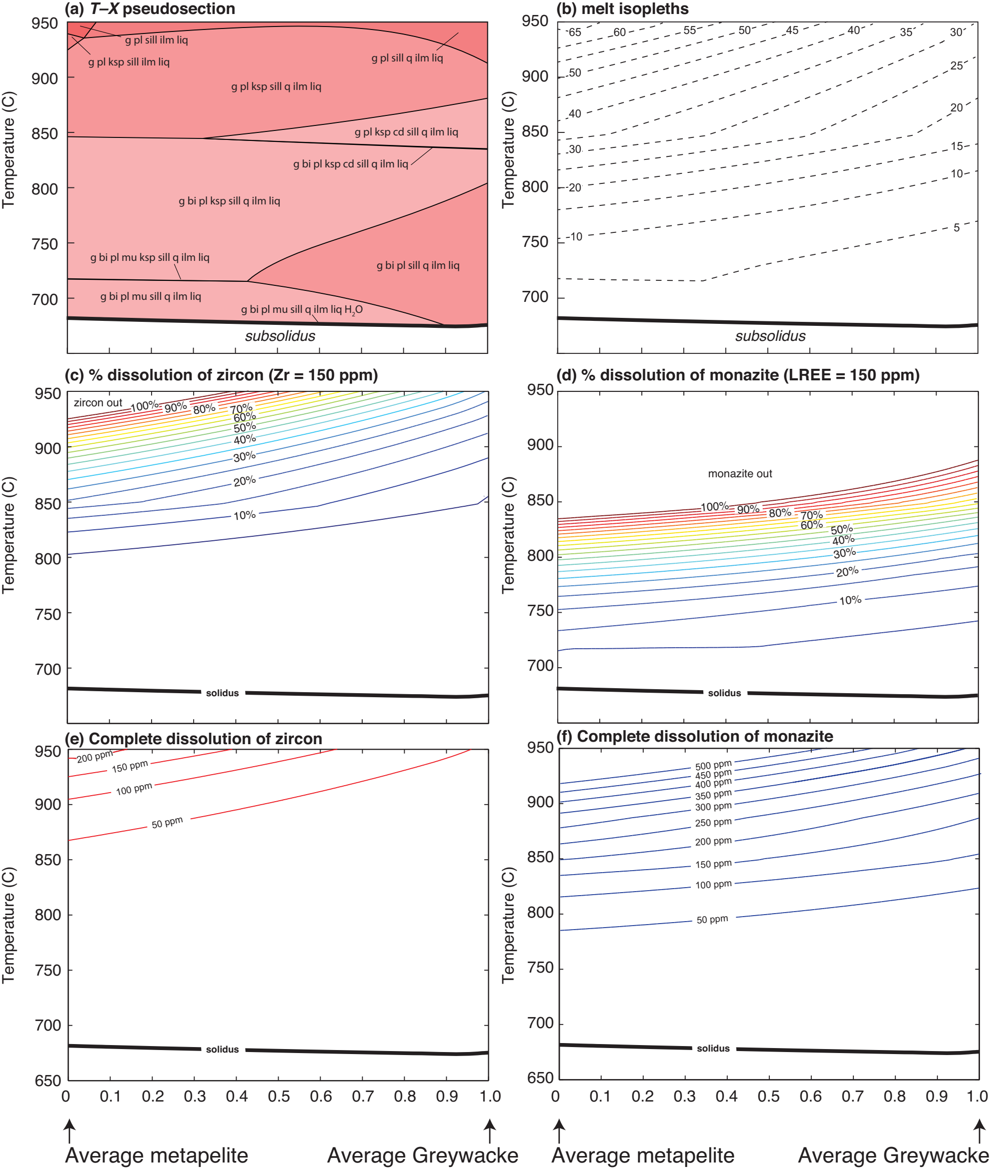
(a) T–X pseudosection
(b) melt isopleths
(c) % dissolution of zircon (Zr = 150 ppm)
(d) % dissolution of monazite (LREE = 150 ppm)
(e) Complete dissolution of zircon
(f) Complete dissolution of monazite
Temperature (C)
950
900
850
800
750
700
650
g pl sill ilm liq
g pl ksp sill ilm liq
g pl sill q ilm liq
g pl ksp sill q ilm liq
g pl ksp cd sill q ilm liq
g bi pl ksp cd sill q ilm liq
g bi pl ksp sill q ilm liq
g bi pl mu ksp sill q ilm liq
g bi pl sill q ilm liq
g bi pl mu sill q ilm liq
g bi pl mu sill q ilm liq H_2O
subsolidus
65
60
55
50
45
40
35
30
25
20
15
10
5
zircon out
100%
90%
80%
70%
60%
50%
40%
30%
20%
10%
monazite out
solidus
200 ppm
150 ppm
100 ppm
50 ppm
500 ppm
450 ppm
400 ppm
350 ppm
300 ppm
250 ppm
0
0.1
0.2
0.3
0.4
0.5
0.6
0.7
0.8
0.9
1.0
Average metapelite
Average Greywacke

Figure 13